Galenic Lab-on-a-Chip concept for lipid nanocapsules production

Nicolas Rolley, Marie Bonnin, Guillaume Lefebvre, Sylvain Verron, Sylwester Bargiel, Laurent Robert, Jérémie Riou, Carl Simonsson, Thomas Bizien, Jean Christophe Gimel, et al.

Galenic Lab-on-a-Chip concept for lipid nanocapsules production

Nicolas ROLLEY[a], Marie BONNIN[a], Guillaume LEFEBVRE[a], Sylvain VERRON[b], Sylwester BARGIEL[c], Laurent ROBERT[c], Jérémie RIOU[a], Carl SIMONSSON[a], Thomas BIZIEN[d], Jean-Christophe GIMEL[a], Jean-Pierre BENOIT[a], Guillaume BROTONS[e], Brice CALVIGNAC[a]

Received 00th January 20xx,
Accepted 00th January 20xx

DOI: 10.1039/x0xx00000x

The continuous production of drug delivery systems assisted by microfluidics has drawn a growing interest because of the high reproducibility, low batch-to-batch variations, narrow and controlled particle size distributions and scale-up ease induced by this kind of processes. Besides, microfluidics offers opportunities for high throughput screening of process parameters and the implementation of process characterization techniques as close to the product as possible. In this context, we propose to spotlight the GALECHIP concept through the development of an instrumented microfluidic pilot considered as a Galenic Lab-on-a-Chip to formulate nanomedicines, such as lipid nanocapsules (LNCs), under controlled process conditions. In this paper we suggest an optimal rational development in terms of chip costs and designs. First, by using two common additive manufacturing techniques, namely fused deposition modelling and multi-jet modelling to prototype customized 3D microfluidic devices (chips and connectors). Secondly, by manufacturing transparent Silicon (Si)/ Glass chips with similar channel geometries but obtained by a new approach of deep reactive ion etching (DRIE) technology suitable with *in-situ* small angle X-ray scattering characterizations. LNCs were successfully produced by a phase inversion composition (PIC) process with highly monodispersed sizes from 25 nm to 100 nm and formulated using chips manufactured by 3D printing and DRIE technologies. The transparent Si/Glass chip was also used for the small angle X-ray scattering (SAXS) analysis of the LNC formulation with the PIC process. The 3D printing and DRIE technologies and their respective advantages are discussed in terms of cost, easiness to deploy and process developments in a GALECHIP point of view.

1. Introduction

Nanomedicine is a steadily growing field in pharmaceutical sciences. It comprises the application of nanotechnologies for the development of new advanced drug delivery systems (DDS). Lipid based and polymer based nanocarriers, inorganic nanoparticles, derived viral vectors and drug conjugates are a few examples of nanotechnologies in DDS currently under development (1–5) or in already marketed (6) drug products. Benefits linked to the use of nanocarriers for delivery of drugs are a decreased degradation of active agents and a reduced toxicity (7–9). These benefits can be explained by the encapsulation of the drugs and/or the improved selectivity of the nanocarriers by active or passive targeting strategies.

Lipid nanocapsules (LNCs), nanoparticles with a liquid lipid-core and a surfactant shell, show strong potentials for both drug delivery and imaging applications (10). They can encapsulate lipophilic molecules, and their size can be tuned from approximately 20 to 100 nm diameter simply by modifying the surfactant-to-oil ratio. Their dynamically arrested pegylated shell offers an excellent colloidal stability in biological media and good stealth properties towards the immune system. All the excipients used in LNCs formulations are generally recognized as safe (GRAS) and biocompatible, and thanks to their lipid composition, they can enhance drug internalization in cells. Moreover, their surface can be functionalized to achieve targeted delivery in specific organs, tissues, and cells (11–13).

To reach clinical applications, control of the physicochemical characteristics, i.e. the shape, the size, the size dispersity, the surface properties (functionalities and charge) and the drug loading of nanocarriers, is mandatory (14). For that reason, the concept of Quality by Design has attracted a growing interest in the development of new nanocarrier based dosage forms (15–17). By defining the target product profile, critical process parameters and their impact on the properties of the final product can be better understood and controlled.

For LNCs, as for other nanoscale DDS, batch production is the most described formulation method in the literature (10,18–26). Drawbacks related to the use of batch processes for production of nanoscale DDS includes “batch-to-batch” variations and difficulties with the scale-up of the formulation procedure (27,28). Together this may hamper the transfer of nano-formulations from the lab to clinical applications.

Therefore, continuous production of DDS assisted by microfluidics (29–36) has drawn a growing interest. Partly because of the high reproducibility of this method, the narrow particle size distribution which can be achieved and the decreased consumption of chemicals. Moreover, microfluidics offers facilities to carry out a high throughput screening of process parameters, to implement online / *in-situ* characterization techniques, and finally to scale-up the production. Several works have shown that microfluidic processes are advantageous in comparison to batch processes, leading to a precise control of critical process parameters (temperature, pressure, concentration, mixing time), resulting in a better control of the formulation characteristics like size and size dispersity (37–41). With all these benefits in mind, microfluidics is here applied to the nanomedicines field as a “Galenic Lab-on-a-Chip” concept.

To date, microreactors are manufactured as microcapillaries or chips using various materials such as polymers, glass or silicon

a. *MINT Lab, UNIV Angers, INSERM 1066, CNRS 6021, Université Bretagne Loire, Angers, France*

b. *LARIS EA7315, UNIV Angers, Angers, Franc*

c. *FEMTO-ST Institute, Univ. Bourgogne Franche-Comté, CNRS, Département MN2S, Besançon, France*

d. *Synchrotron SOLEIL, Gif-sur-Yvette, France*

e. *IMMM, CNRS UMR 6283, Le Mans Université, Le Mans, France*

† Footnotes relating to the title and/or authors should appear here.
Electronic Supplementary Information (ESI) available: [details of any supplementary information available should be included here]. See DOI: 10.1039/x0xx00000x

(Si) (42). The choice of the material depends on operating conditions such as pressure and temperature, chemical compatibility, cost, and ease of fabrication (43,44). Compared to microcapillaries, microfluidic chips offer the possibility to tune and optimize the mixing efficacy thanks to a large choice of micromixers, channel designs and structures. To achieve an optimal mixing of various ingredients, different active or passive micromixers systems are used for nanoparticle formulations (45–48). Focusing on passive micromixers, Y-type, T-type, Cross-type or Flow focusing-type junctions are currently used. The mixing phenomena can be completed with possible streamline disturbances like zigzag, chicanes or serpentines inside the channels. Chips also provide the opportunity to easily miniaturize and thermalize the devices. They can be made of polydimethylsiloxane/Glass or Si/Glass. These materials can be chosen for their optical properties to easily implement characterization techniques like X-Ray scattering (49). Despite a growing interest during the last decade, microfluidic chips can still be very expensive and difficult to produce. For instance, manufacturing methods such as soft lithography and micro-etching require specific skills and equipment (like cleanrooms for silicon etching) that are not widespread in a standard research laboratory. Moreover, considering the multitude of possible chip designs to manufacture, in terms of dimensions, inlet/outlet numbers and positions, transparent measurement windows, these chip systems require specific holders and connectors. Hence, 3D printing technology has gained increasing attention to fabricate chips and holders including fluidic and electric connections (50,51). However, to the best of our knowledge, only a few studies have investigated the use of 3D printed chips for nanomedicine formulation, and all were made of polylactic acid (52–54).

In this context, we propose to spotlight the “Galechip” concept through the development of an instrumented microfluidic platform considered as a “Galenic Lab-on-a-Chip” (for pictures and details, see SI section S1). With this platform, LNCs are for the very first time produced by microfluidics thanks to a low energy phase inversion composition (PIC) process (55). The “Galechip” concept relies on (i) the technological development and prototyping of microfluidic reactors and connectors in order to rationally develop the formulation process and the production of LNCs, and (ii) the *in situ* integration (or as close as possible to the formulation) of characterization techniques (like X-ray scattering) in order to better understand the not yet fully elucidated physicochemical mechanisms involved in the formation of LNCs. The intended purpose is to have a better understanding of the production of such nano-DDS candidates that will impact their biological behavior. Yet, biological studies of such formulated LNCs are beyond the scope of this paper and will not be presented here. Indeed, preclinical investigations on similar LNCs produced by batch phase inversion processes are already the core of many studies published by our group and others (10,19–23,25,56,57).

The present work reports the applicability of two common additive manufacturing techniques, namely fused deposition modelling (FDM) and multi-jet modelling (MJM). Regarding the FDM technique, two materials have been selected, i.e. poly ether ether ketone (PEEK) for its solvent compatibility and strong mechanical properties and acrylonitrile butadiene styrene (ABS) for its low cost and low melting temperature. The MJM was used for the acrylic resin printing of holders with chip connectors and the integrated thermalization system for the chip temperature control. Moreover, for the very first time, a new deep reactive ion etching (DRIE) technique has been tested to produce Si/Glass chips with deeper channels. The objective was to increase the X-ray scattering volume and thereby the signal-to-noise ratio using synchrotron X-ray beams.

All the chips (PEEK, ABS and Si/Glass) have been tested for the production of LNCs by the PIC process, using an on purpose developed microfluidic platform. Besides, the transparent Si/Glass chip has been used to evaluate its potential for the formulation process analysis by small angle X-ray scattering (SAXS).

2. Materials and Methods

2.1. Si/Glass chip

2.1.1. DRIE microfabrication process

DRIE is a highly anisotropic process of plasma etching, commonly used for wafer-level microfabrication of various structures in silicon, e.g. trenches, cavities and channels (58). DRIE provides significant advantages when compared to other etching methods as it enables the fabrication of high aspect ratio features with vertical sidewalls over relatively high depth range (typ. <500 µm) and with high etch rate (typ. >10 µm/min). In the field of microfluidics, DRIE is frequently used for single- or double-side etching of Si substrates to form microchannels and via-holes. Further, anodic bonding of such structured Si substrates to glass lids allows relatively simple fabrication of even complex Si/Glass or Glass/Si/Glass devices.

All DRIE processes were made using an ICP Pegasus Rapier reactor (SPTS, United Kingdom) on 4”, (100)-oriented p-type silicon wafers (Sil’tronics, France), having 1.8 mm of thickness. Due to the high depth of silicon channel (1.5 mm for scattering experiments), a standard two-step Bosch process (59) could not be used for reasons explained below. An STS Advanced Silicon Etch ASE® process was carried out instead. This is a modified three-step Bosch process, allowing better control and higher etching performances. Anodic bonding of silicon structures to 0.5 mm thick Borofloat® 33 glass wafer (Schott, Germany) was performed on an EVG501 wafer bonder (EVG, Austria). Figure 1 gives a schematic of the fabrication process flow-chart resulting in relatively simple structures with microchannels and via-holes, formed by two subsequent combinations of photolithography and dry etching, on top (Fig. 1A to 1D) and bottom side (Fig. 1E to 1H) of the wafer, respectively. Here, a combination of 1 µm-thick thermal SiO_2 and 24 µm-thick AZ® 9260 photoresist was used (Fig. 1A and 1B). The SiO_2 layer was dry etched using a DRIE method to ensure vertical profile of the sidewalls.

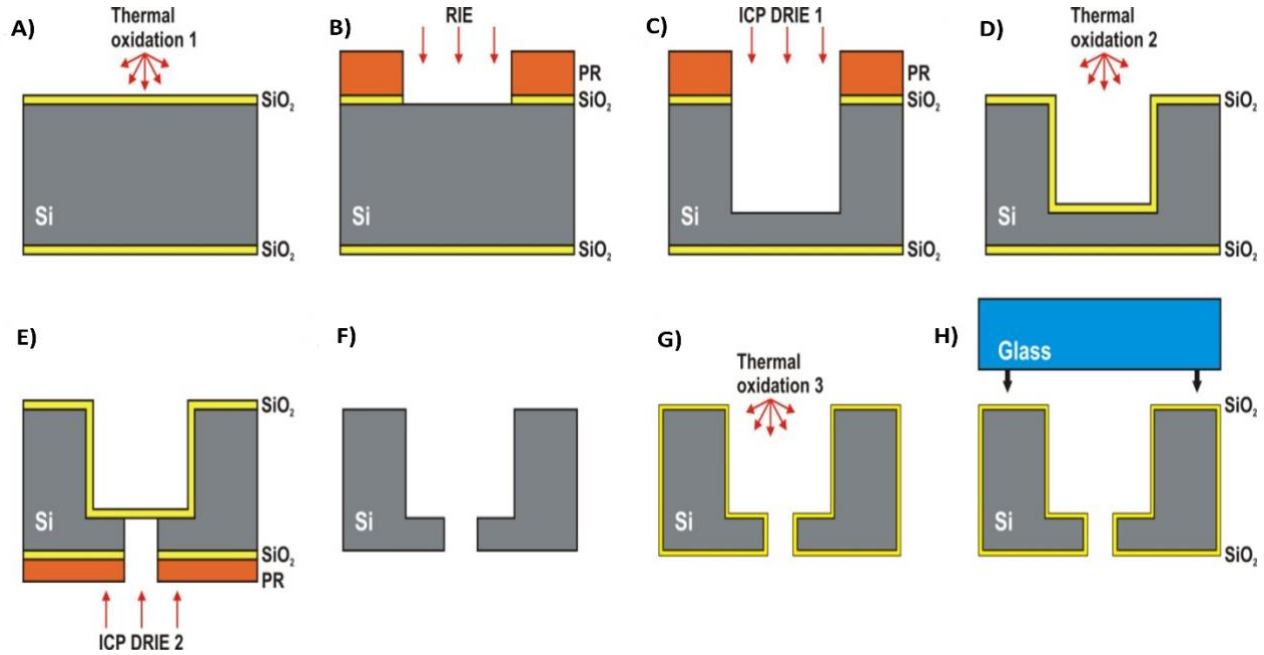

Fig 1: Fabrication process of Si-Glass microfluidic chip, combining the DRIE of silicon and anodic bonding: A) Thermal oxidation of Si, B) photolithography and dry etching of SiO_2 mask, C) DRIE of microchannel, D) stripping of the masks and second thermal oxidation, E) back-side DRIE of via-holes, F) stripping of the masks, G) thermal oxidation (Si surface passivation), and H) anodic bonding to glass lid.

As mentioned previously, the standard two-step Bosch process, which employs two alternative cycles of C_4F_8/SF_6 plasma (Passivation/Etch) with fixed (not changing in time) etch parameters, is not effective in this case because of relatively low etch rate and progressive deterioration of etching quality when exceeding 400-500 µm depth. Therefore, the ASE® process was employed, which is a modified three-step Bosch process (Passivation/Etch1/Etch2), based on C_4F_8/SF_6 chemistry. Etch1 step refers to a highly directional (energetic) removal of a passivation layer, very effective at the bottom of the channel, whereas Step 2 refers to classic isotropic Si etching. Moreover, ASE® with variable (changing in time) process parameters was developed to keep a stable etch rate of ~8 µm/min and to ensure good sidewall quality during whole DRIE1 process (Fig. 1C). After etching, the mask layers were removed, followed by a cleaning procedure to prepare the wafer for wet thermal oxidation (Fig. 1D). Thin 0.2 µm SiO_2 layer was grown in order to protect the channel surface from the SF_6 plasma during subsequent via-holes formation by back-side DRIE2 process (Fig. 1E and 1F). After this step, the silicon wafer was cleaned and oxidized again to 0.13 µm in order to obtain smoother and more hydrophilic surface in the channels (Fig. 1G). Finally, an anodic bonding of processed silicon wafer to blank (unprocessed) 0.5 mm thick Borofloat®33 glass wafer (Fig. 1H). Both wafers were cleaned in a Piranha solution (H_2O_2:H_2SO_4, 1:3) and rinsed in deionized water in order to obtain clean and hydrophilic surfaces. The anodic bonding was carried out in EVG501 bonder under vacuum (1.8×10^{-3} mbar) at 350°C by applying the high voltage sequence of 300/600/900/1,100 V and bonding force of 700 N (compensation of wafer bow).

The manufactured chip had a surface of 26 × 40 mm and a thickness of 2.3 mm. Microfluidic channels included two liquid inlet channels, connected with a 90° "Y-shape" followed by a unique mixing channel. The channel section was 300 µm width and 1,500 µm depth, and the mixing channel was designed with six hundred and seven 90° elbows with a total length of 500 mm from the mixing point. All specifications of Si/Glass chips are summarized in Table S2-1 and an overall view is presented in Figure S4-1 in the SI.

2.1.2. Channel characterization of the microfabricated Si/Glass chips

A VHX-7000 digital microscope (Keyence Corporation, Osaka, Japan) equipped with a Z20 (20-200x) objective (Keyence Corporation, Osaka, Japan) was used to check the verticality and to measure the depth (D) and width (W) of channels and 90° elbows. The Si/Glass chip has been illuminated by visible light, and multiple stacked images were taken and analyzed with the software Keyence VHX-7000 to obtain 3D images of the channel geometry.

Depth and width non uniformity (dNU% and wNU%, respectively) were determined with the following equations:

$$dNU\% = 100 \times \frac{(d_{max} - d_{min})}{(2 \times d_{mean})} \quad (1)$$

$$wNU\% = 100 \times \frac{(w_{max} - w_{min})}{(2 \times w_{mean})} \quad (2)$$

The sidewall surface of chips has been qualitatively characterized with FEI ESEM Quanta 450 FEG scanning electron microscopy (FELMI-ZFE, Graz, Austria).

2.2. PEEK and ABS chips

2.2.1. 3D printing manufacturing

The additive manufacturing of ABS (Verbatim Gmbh, Eschborn, Germany) and PEEK (Apium Additive Technologies Gmbh, Karlsruhe, Germany) chips require four steps detailed in supporting information S2: (A) the modelling with a CAD

software, (B) the slicing step, (C) the printing of the model and (D) finalizing step with milling and smoothing.

2.2.2. Channel Characterization of the 3D printed chips

To observe the geometry of the channel interior, i.e. verticality, width and 90° elbows, with a digital microscope (Keyence VHX-7000, Keyence Corporation, Osaka, Japan), the printing process was stopped at a 1,500 µm hight. Thanks to the PEEK autofluorescence (60), confocal laser scanning microscopy (CLSM) was also used to check the verticality and the deformation inside channels and 90° elbows of the PEEK chip. Different regions of interest (ROI) of the chips were characterized using a Leica TCS SP8 CLSM (Leica Microsystems, Heidelberg, Germany) with an HC PL FLUOTAR 10X (N.A. 0.30) and × 0.75 zoom. The excitation wavelength was 405 nm and emission was detected between 409 to 784 nm. Multiple stacked images (1,024 × 1,024 pixels) were taken at 400 Hz with x, y and z spatial resolution of 1,515 µm, 1,515 µm and 5 µm, respectively.

2.3. Chip Plugging and heating devices manufactured by 3D printing

An "all-in-one" plugging and heating device has been designed for the integration of Si/Glass, PEEK and ABS chips, and prototyped in two parts (Fig. 2A and Fig S3-1 in the SI). Due to the similarity between the heating part (part (1) in Fig. 2A and 2B) and the waterblock technology used for the water cooling of a central process unit, our device will be called "waterblock" in the following. Details are given in supporting information S3.

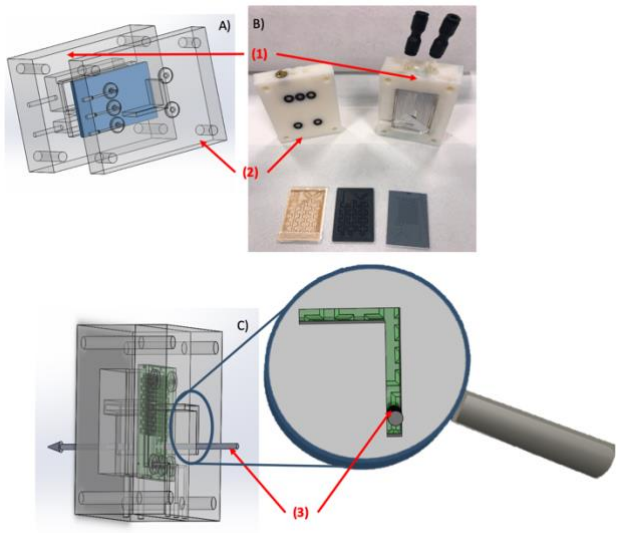

Fig 2: "All-in-one" plugging and heating device. CAD drawing (A) and picture (B) of the heating part called "waterblock" (1) and of the connector part (2). SAXS implementation (C) with the representation of the X-ray beam path (3) (see section 2.5.2. SAXS analysis for more details).

Different sealing and pressure tests were performed on 3D printed microfluidic chips. To check the integrity of the PEEK channels and the absence of leaking between the deposited filaments, colored water with a blue dye was injected inside the chip under nominal flow conditions to visually check the whole chip by transparency. In addition, the maximum tolerable liquid pressure in the chips was evaluated by increasing the pressure until the appearance of leaks on chip sides or inlet and outlet connectors. In practice, one over the two inlets was plugged to a pressure syringe pump (Teledyne Isco, model 100DM, Lyncoln, USA) and the other inlet and the outlet were clogged. A flow target was set at 100 µL/min. Then a pressure plateau was monitored, until a leak appeared at constant pressure.

2.4. LNC formulation

2.4.1. Materials

Nonionic surfactant Kolliphor® HS 15 (mixture of free PEG 660 and PEG 660 12-hydroxystearate, HLB ~ 14–16) and co-surfactant Span®80 (sorbitan monoleate, HLB ~ 4–5) were respectively provided by BASF (Ludwigshafen, Germany) and Sigma-Aldrich Co. (Saint Quentin Fallavier, France). Labrafac® Lipophile WL1349 (medium-chain triglycerides) was purchased from Gattefossé (Saint-Priest, France). These three ingredients are respectively called Kolliphor, Span and Labrafac in the following sections. Ultrapure water was obtained from a MilliQ filtration system (Millipore, Saint-Quentin-en-Yvelines, France).

2.4.2. Phase inversion composition process

The LNC formulation is based on the phase inversion composition (PIC) process, previously developed using a batch process with the same excipients (61). Basically, the oil, surfactant and co-surfactant were mixed at 37°C, leading to reverse micelle type structures as PEG blocks of Kolliphor are insoluble in Labrafac alkyl chains. Then, water at room temperature was added, resulting in its diffusion within reverse structures where it hydrates PEG blocks. The increase of water content in the system induces the progressive swelling of the reverse structures until the inversion of the oil/water interface curvature, finally resulting in the spontaneous formation of the LNCs after having crossed a microemulsion state (62). Due to the spontaneous nature of this process, it was named spontaneous nano-emulsification by Lefebvre *et al. (61)* and the obtained nano-objects were named lipid nanoemulsions (LNE). To avoid any misunderstanding with other spontaneous emulsification methods without any change in the interface curvature (63), the more appropriate term PIC is used here. Besides, the LNC term is preferred to LNE because of the core-shell structure proposed by Heurtault *et al.* (18), which is supported by SAXS results from this work, and their high stability (at least one month) even after dilution under the critical micellar concentration (data not shown in this study).

In the present work, the LNC formulation by the PIC method in microfluidic Formulation Process (µFP) and Batch Process (BP) were performed at 37°C for the oily phase and room temperature for added water. A temperature of 37°C was sufficient to ensure a homogeneous mixing between surfactants and oil.

Different LNCs were prepared with various surfactants-to-oil mass ratios and different co-surfactant-to-surfactant mass ratios, i.e. Span-to-Kolliphor mass ratios (Table 1). Only one surfactants and oil-to-water mass ratio (SOWR, Eq. (3)) of 0.05 was tested.

$$SOWR = \frac{mass_{Kolliphor} + mass_{Span} + mass_{Labrafac}}{mass_{water}} \quad (3)$$

The feasibility study of LNC formulation by µFP was performed using a home-made formulation pilot developed for this purpose (see the SI section 1) and equipped as follows:

- An OBI MK3 pressure controller (Elveflow, Paris, France) for flow circulation.
- Glass bottles and PEEK capillaries for oil and water storage and feeding by pneumatic transport (Ø 1 mm and Ø 0.5 mm respectively).
- A MFS5 flowmeter (Elveflow, Paris, France) for oil flow rate control.
- A Mini Coriolis M14 flowmeter (Bronkhorst, AK Ruurlo, Netherlands) for water flow rate control.
- A 40 psi and a 75 psi back-pressure regulator cartridges (Idex Health&Science LLC, Lake Forest, USA), respectively for the oil and water feeds, used as fluidic resistances to work in the optimal pressure range of the pressure controller.
- A water bath for the temperature control of the oil supply (heated with a counter-current tubular heat exchanger system) and of the waterblock (to heat the microfluidic chip).
- The microfluidic chip was inserted between the connector part and the waterblock.

Table 1: Compositions of the oil phase for the formulation of three different sizes of LNCs

	Weight fraction (%)		
	Labrafac® W L1349	**Kolliphor® H S 15**	**Span® 80**
LNC 25 nm	25	65	10
LNC 50 nm	40	50	10
LNC 100 nm	55	45	0

Besides, two oil flowrates of 100 µL/min and 500 µL/min were tested with water flowrates of respectively 2,000 µL/min and 10,000 µL/min, to keep the SOWR constant as previously mentioned. Each time, 3.5 mL of the suspension were collected and further diluted for dynamic light scattering (DLS) size measurements (see section 2.5.1). The formulation reproducibility was tested on size measurements with three independent oil phase preparations (3 different weightings and mixing) per composition. The process repeatability was tested for each composition with three "start and stop" of the oil and water flowrates with complete cleaning of the chip with water between each run. Finally, 9 measurements were performed for each composition.

2.5. Characterization techniques

2.5.1. DLS and statistics data analysis

LNCs z-average hydrodynamic diameter (D_{Hz}) and polydispersity index (PDI) of each experimental point were determined by a Zetasizer Nano S device (Malvern Panalytical, Malvern, United-kingdom). DLS measurements were performed after a dilution in ultrapure water at 25°C. The helium–neon laser, 4 mW, operates at 633 nm, with a fixed 173° scattering angle. The position of the scattering volume was set at 4.85 mm from the PMMA cuvette wall and samples were sufficiently diluted to suppress multiple scattering and to obtain attenuator values from 8 to 9. Data were collected and analyzed using the Malvern Zetasizer software version 7.11 and D_{Hz} and PDI were calculated from the autocorrelation function of the scattered light, using the cumulant analysis (64).

To compare the D_{Hz} of the LNCs formulated with the Si/Glass and PEEK chips, Passing-Bablok regressions were performed (65). In comparison with a classical linear regression, Passing-Bablok regression is a statistical method for non-parametric regression. It is a robust process, non-sensitive to the error distribution and to the data outliers. This regression checks that two different methods lead to the same result: for two variables Y_i and X_i linked by a linear relationship (Eq. 4), Passing-Bablok regression will assess if 0 is included in the 95% confidence interval (CI) of α and 1 is in the 95% CI of β. The linearity between the two variables is generally controlled using the CUSUM test (cumulative of the scores), which measures the stability of the model over the entire region of interest.
If 0 is not included in the 95% CI of α, there is a systematic error between the two methods, while if 1 is not in the 95% CI of β, there is a proportional error.

$$\widehat{Y}_i = \alpha + \beta X_i \quad (4)$$

In the present work, the two studied variables, Y_i and X_i, reflect each D_{Hz} of the LNCs formulated respectively with the PEEK and the Si/Glass chip. The Si/Glass chip has been selected as the reference process (X_i) due to the best control of the width and wall linearity of its channels.
Moreover, a Bland-Altman plot has been used to analyze the agreement between the two sets of data. The aim of this statistical test is to compare two sets of quantitative values obtained by two different methods (66) and to infer possible biases or outliers. In this case, the two methods are the two different chips (Si/Glass and PEEK) used for the LNC formulation, and the D_{Hz} was used as the comparative value. In practice, the difference in D_{Hz} obtained with the two methods $(X_i - Y_i)$ is plotted as a function of the average $(X_i + Y_i)/2$ and the test consists in controlling that all points are within the 95% CI of the differences and homogeneously distributed around the average of the differences.
The same methodology (Passing-Bablok regression and Bland-Altman plot) was used to compare results from two flow rates in a same PEEK chip.

2.5.2. Small Angle X-ray Scattering Experiments

For the SAXS measurements, the microfluidic formulation pilot, with the Si/Glass chip; was mounted on the SWING beamline at SOLEIL synchrotron (Saint Aubin, France) with our "Galechip" environment designed for a continuous formulation (Fig. 3A). In order to carry out *in situ* SAXS characterizations of the LNCs produced by the PIC process, the X-ray beam had to cross the silicon wafer and glass cover of the microfluidic chip (Fig. 3B). Different flow rate conditions (up to 10,000 µL/min) were tested with an optimal beam position in the middle of the channel to avoid intense side wall reflections at grazing X-ray incidences. The X-ray beam impinged the silicon wafer wall at normal incidence and went through 300 µm of silicon before being scattered by the sample solution within the etched microchannel. X-ray scattering was then transmitted through 500 µm of glass, few millimeters of air and finally through the window that closed the detector vacuum tube. The synchrotron beam was focused on the detector beam stop set in front of the detector at 2 to 6 m away from sample, using Kirkpatrick-Baez X-ray mirrors and collimating slits. Dimensions of the 12 keV monochromatic beam were measured from a so-called "sample

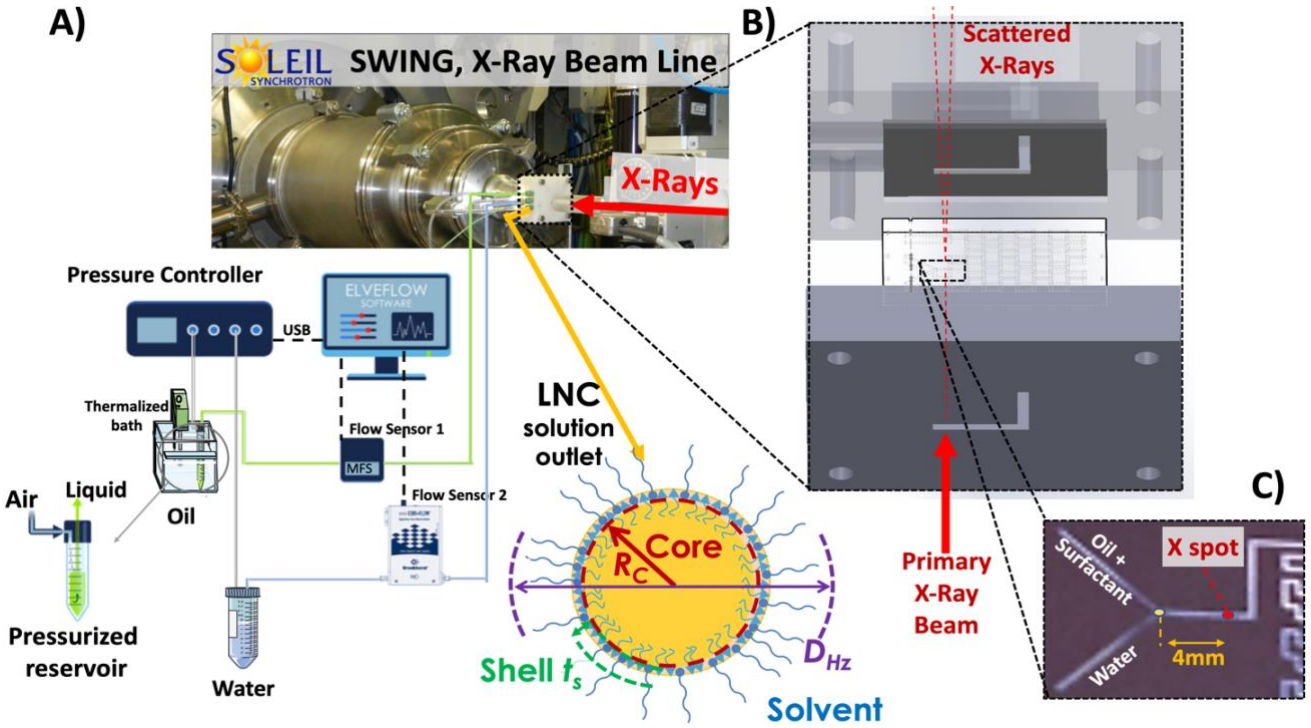

Fig 3: A) Integration of the microfluidic formulation pilot in the SAXS environment at the SOLEIL synchrotron SWING beamline for *in situ* characterization of the LNC structure and their characteristics as the shell thickness (t_s), the hydrodynamic diameter (D_{Hz}) and the core radius (R_c) ; B) Representation of the microfluidic setup composed of the chip mounted inside the waterblock connector and C) Position of the X-ray beam.

blade scan" using the silicon sample edge: 200 µm in width (horizontal dimension) and 80 µm in thickness (vertical dimension). Since X-ray scattering occurring from the chip materials could be an issue, the signal/noise ratio was optimized setting the EIGER X 4M detector gain to 4 for the microfluidic cell measurements while it was set to 1 for classical glass capillary measurements measured at 2.5 m (sample to detector distance).

3. Results and discussion

3.1. Microfluidic chips design

Many geometrical designs exist for passive microreactors and were adapted to the Galechip concept, with nanomedicines formulation and *in situ* characterization. As previously mentioned, in order to obtain a sufficient scattering volume for a good signal-to-noise ratio for scattering experiments, a channel depth of 1.5 mm was used for the chips. This was an important technical challenge that required innovations to adapt the DRIE technology to the fabrication process of transparent Si/Glass chips (detailed in section 2.1.1). A Y-type junction has been chosen, despite its limited mixing capabilities, to minimize the number of connections and for its ease of implementation. Thus, the microfluidic chip combines two fluid streams (oily solution and water) without turbulence, which to some extent will flow parallel in the channel with diffusive mixing (67). 90° elbow chicanes were designed and as many as possible were integrated on the chip to induce an optimal mixing and channel length for each chip design.

3.1.1. Si/Glass Chip characterization

DRIE fabrication strategy was used in this work to manufacture Si/Glass chips. However, as already mentioned, high depth microchannels (1.5 mm) make the first etching step very challenging. Indeed, it requires not only significant improvement of the DRIE etching performance but also a selection of the hard mask, followed by careful optimization of the photolithography parameters, in order to ensure a thermally and mechanically stable masking layers with smooth and vertical sidewalls that could survive a long etching.

Etched microchannels have been analyzed in terms of depth/width uniformity and surface quality. Measurements were realized on two different chips, the first set on the Si/Glass chip used in the experiment and the second set on a silicon chip without glass cover but manufactured on the same wafer. This second chip without glass cover was used as positive control in order to confirm the absence of glass interference during measurements, given the repeatability of the etching process validated on different chips (not shown here). Silicon chip showed an average depth of 1,500.2 ± 26.8 µm and an average width of 277.5 ± 3.5 µm. The measurements on the Si/Glass chips, e.g. with or without glass cover, suggested the absence of difference between both chips, thus the following presented measurements are those performed on the used chip. Figures 4 and 5A shows results obtained on depth characterization for Si/Glass chip at different ROI (more results are presented in Fig. S4-1 and S4-2). The depth dispersion observed on the structure level reached 124.8 µm. As expected, the deepest measure was obtained at the outlet (in an unobstructed area: ROI 4, 1,546.7 µm) while the shallowest was in the center of the chip (ROI 5, 1,421.9 µm). This corresponds to a max-min depth non-uniformity dNU% of 4.2%. The deviations can be explained by local variation of the mask pattern density: higher density of exposed Si leads to a local depletion of reactive species, and hence, local reduction of etch rate (microloading effect). This local variation of etch rate is responsible for the corrugation of the bottom surface, especially in the 90° elbows (Fig. 4A). This phenomenon was known, and several remedial actions were undertaken anticipatory to combat this aspect, mainly based on optimization of the mask design but also by adjusting the

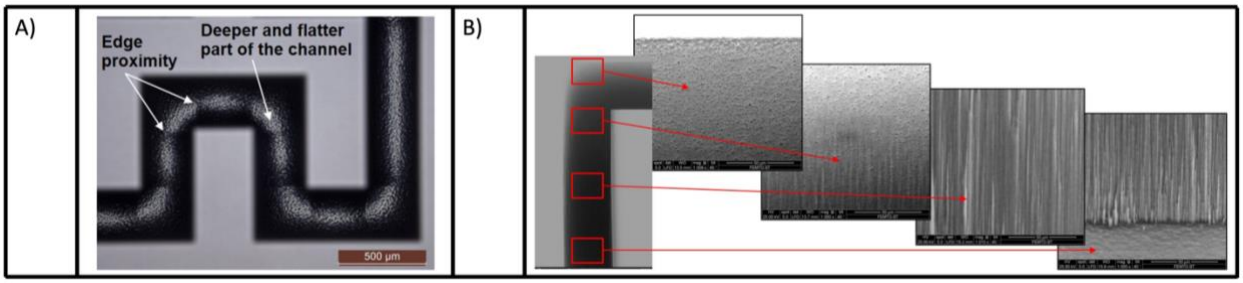

Fig 4: SEM pictures for the characterization of the microchannel in terms of depth uniformity and surface quality: A) Corrugation of the bottom surface due to very local variation of etch rate, B) Evolution of the sidewall quality along the total depth of 1.5 mm (SEM tilted view).

flow rate of process gases during the DRIE1 step (Fig. 1C). The very good dNU% obtained (< 5%) proved their efficacy.

Regarding the width, the same analysis was performed, but considering the difficulty to wash the channel chip, wNU% was a little bit more important with a value of 8.5%. The average width was 261.1 ± 34.7 µm. This deviation can be explained by a thin liquid layer at the surface of the wall that the software has assimilated to silicon, which reduced the calculated channel width.

In addition to the width, non-uniformity analysis measurements of the wall verticality were performed, and the results showed a very good uniformity of the wall verticality with value of down angle between 88.2° and 93.6°. Sidewall surfaces of the fabricated microchannel were visualized by SEM along its total depth of 1.5 mm (Fig. 4B). The flat surface with increased roughness can be found to about half of the microchannel depth. Vertical roughness along the sidewall, so-called striations, started to appear deeper, indicating insufficient removal of the passivation layer. Striations were developing with the etch depth leading finally to significant vertical roughness as well as to small profile deformations at the bottom. This effect can be decreased by further optimization of the etch process. Post-processing surface treatment can also be performed directly after DRIE1 process (Fig. 1C) in order to "polish" the sidewall surface (e.g. by short wet etching in hot KOH etchant), while protecting other surfaces from aggressive KOH by a thermal oxide layer.

3.1.2. ABS Chip characterization

Characterizations of the ABS chip by depth, width and wall verticality measurements have been performed using digital microscopy (Fig. 5B and SI Fig. S4-3). Measurements in different regions of interest showed significant depth differences between external left lower (ROI 2_{lower}) and external left upper channels (ROI 2_{upper}) (ROI 2_{lower} = 1,698.63 µm and ROI 2_{upper} = 1,496.81 µm). This corresponds to a dNU% of 6.3%. Concerning the width, wNU% could not be estimated since it was difficult to define precisely by "eye" the wall position due to their lack of surface flatness. Indeed, microscopy observation showed the existence of many deformations inside the channel. This could be explained by the difficulty to control the linearity of the nozzle x-y motion with only a precision of about 120 µm (68), which corresponds to 8.0% of the depth and 20.0% of the width. Another explanation could be the absence of a fully enclosed chamber over the printer, which could have improved the printing quality by decreasing the warping phenomena that induced deformations inside and outside the chip.

3.1.3. PEEK Chip characterization

First, a leaking control was performed with the injection of blue colored water. The transparency of the chip under high-intensity white light, resulting from a 60% fill rate during printing, made it possible to observe that there was no leakage of blue water outside the channels.

The PEEK chip was also characterized using the same method as the ABS chip with the digital microscope observations. The channel wall verticality was slightly different from Si/Glass chip, with left mean

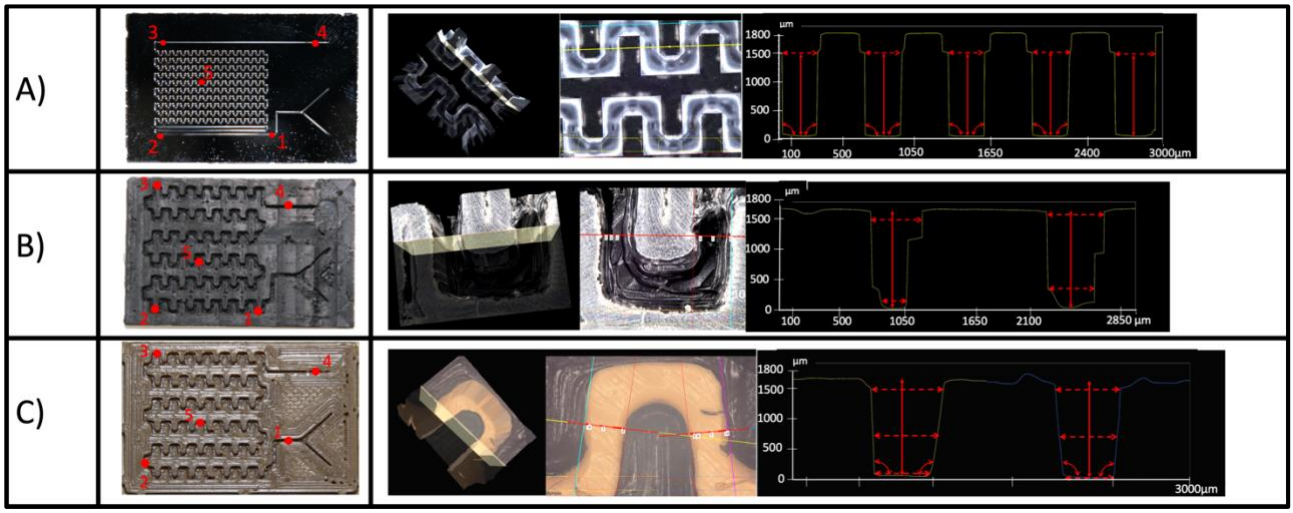

Fig 5: 2D/3D microscopic observations of 90° elbows of A) the Si/Glass chip, B) the ABS chip and C) the PEEK chip. Each Region Of Interest (ROI) are presented for each chip and numbered from 1 to 5. Each chip was observed on the RIO number 5 on this present example.

angle about 94° and right mean angle about 89°. Thus, two measurements of the wNU% were carried out along the channel height, upper and lower, leading to w_{upper}NU% = 22.9%, w_{lower}NU% = 12.7% and dNU% = 2.9% (Fig. 5C and SI Fig. S4-4). The w_{upper}NU% was about 22.9% (ROI 3 = 516.9 µm, ROI 2 = 321.6 µm) which is in the same order of magnitude than for the ABS chip. The w_{lower}NU% was about 12.7% (ROI 2 = 400.2 µm, ROI 1 = 309.9 µm) indicating a better control of the width at the beginning of the printing process. This wNU% could be explained by a 370°C difference between the PEEK extrusion temperature (480°C) and the print bed temperature (110°C), inducing a possible retraction of the polymer and a deformation of the chip structure. These structural defects could cause internal fluid leakages. Concerning the dNU%, measurements in the different ROI showed a low dispersion of depth between external right upper and central channels (ROI 4 = 1,600.3 µm and ROI 2 = 1,510.3 µm respectively), which is in the same order of magnitude as the Si/Glass chip.

As already mentioned, the autofluorescence of the PEEK material enabled a 3D observation of chips by CLSM. Different regions, including three of the ROI characterized by digital microscopy, have also been observed by CLSM. Two of the observed ROI are presented in the supporting information (section S5). These observations confirmed dNU% and wNU%. Verticality checking can also be performed by CLSM, but the limited depth of field does not allow a direct observation over the entire height of the channels. Thus, the chip has been milled to reach the bottom of the channels, making it a destructive characterization method.

3.2. LNC microfluidic formulation

The main challenge for the transposition from the PIC batch process to a continuous process was the control of hydrodynamic process parameters. Indeed, it was observed that the water diffusion rate inside the oil phase can be influenced by the water injection rate and mixing conditions (69). Thus, microfluidics seems an appropriate solution as it allows precise control of the water injection rate and the chip can be designed to optimize the mixing.

In order to overcome difficulties associated with hydrodynamic parameter control, LNC BP were formulated as references using the well-known batch process. For each targeted size (25, 50 and 100 nm), three different batches of oil/surfactant mixtures were prepared, called stock solutions. Using each oily stock solution, LNC µFP were formulated with the three different chips (except for ABS chip that was only tested with one stock solution). Thus, for each targeted size, 24 formulations were performed (Fig. 6):

- 3 BP formulations (one with each stock solution): the average D_{Hz} and PDI obtained were used as references.
- 3 µFP formulations with the ABS chip: three “start and stop” for one stock solution.
- 9 µFP formulations with the PEEK and with the Si/Glass chip: three “start and stop” for each of the three stock solutions.

The percentage deviations between D_{Hz} and PDI of the LNCs formulated with the µFP (with the three types of microfluidic chips) and BP are presented in Figure 6. Firstly, it should be noted that for all three different targeted sizes, LNCs were obtained with good monodispersity (0.015 ≤ PDI ≤ 0.129) and sizes between -15% and +25% of those obtained with BP. Secondly, according to the targeted size, the same chip sometimes leads to slightly smaller or slightly larger LNC µFP than LNC BP: within these small deviations, no clear trend was identified yet. Finally, for most of the formulations, PDI was smaller with µFP than with BP. This is consistent with Abstiens *et al.* (70), who stated that there is a contribution from the microfluidic process that improves tightening of size distributions in comparison to BP.

This comparison of three different chips with a batch process formulation is important to demonstrate the interest of using microfluidics to carry out the transposition and the scale-up from a batch to a continuous process to produce nanoparticle based medicinal products as LNCs (14).

To go further in this work and to validate the Galechip concept using PEEK chips for the formulation/production of nanomedicines and using Si/Glass chips for their *in-situ* characterization, a comparative statistical study was carried out. It was done using Passing-Bablok and Bland-Altman statistical methods comparing D_{Hz} obtained with PEEK and Si/Glass chips.

Indeed, a specific high-light of these two chips is of interest because

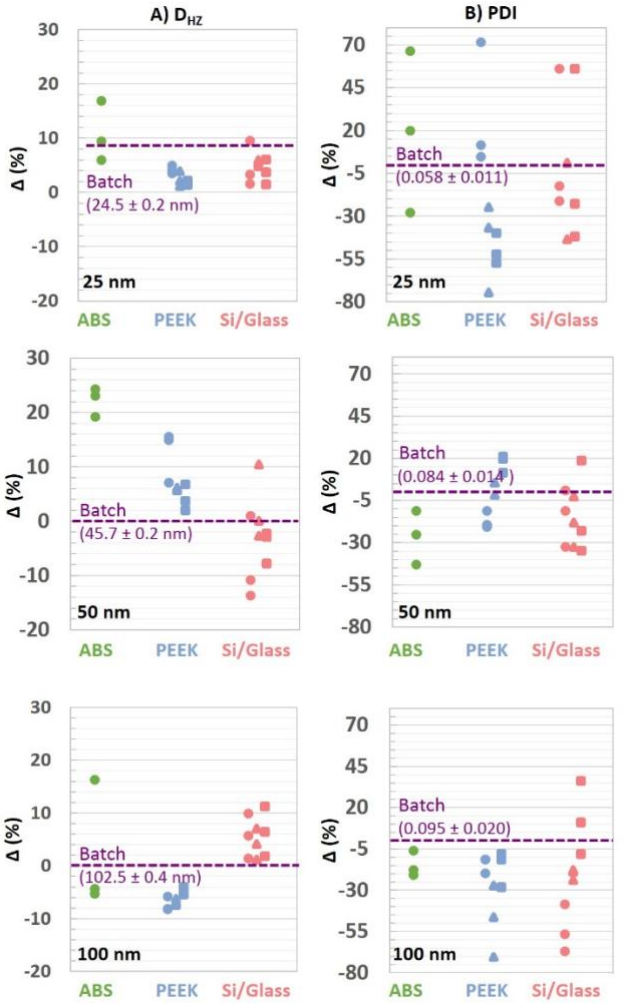

Fig 6: Comparison of (A) D_{Hz} and (B) PDI for three targeted sizes indicated in the figures (25, 50 and 100 nm) using the PIC batch and microfluidic processes. Results obtained with the batch process are used as references (purple dashed lines). Results obtained with the three different chips are represented with different colored symbols: ABS (green), PEEK (blue) and Si/Glass (pink). Independent organic stock solutions were prepared for each targeted size and are represented by various symbols (circles, triangles, squares) with three “start and stop” for each one.

of their complementarity in the Galechip concept: 3D printing technology allows the manufacture of very low cost chips (a dozen of euros each) while DRIE technology (many hundreds of euros per chip,

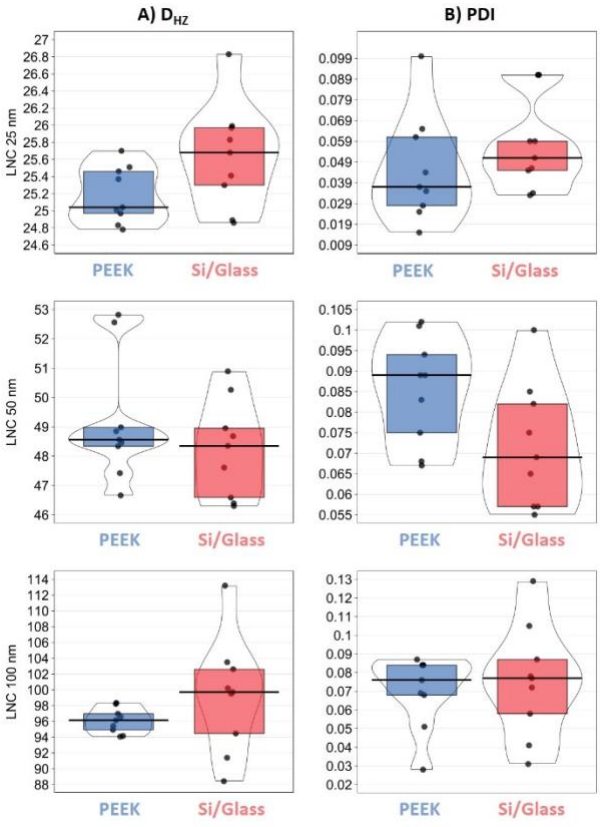

Fig 7: Violin plots of (A) D_{HZ} and (B) PDI for LNC formulations obtained with PEEK (blue) and Si/Glass (pink) chips. Each boxplot introduces four elements: black points represent raw data, the horizontal black line represents the median, the bean represents a smoothed density and colored rectangles represent the interquartile range.

without taking in consideration the need of a clean room) provides Si/Glass chips adapted for *in-situ* studies of LNC formation (see section 3.3 SAXS Results).

ABS chip will not be further investigated in this work, as this material is less compliant than PEEK for pharmaceutical use (poor compatibility with solvents, poor mechanical and thermic resistance, etc.). However, it was interesting to confirm its feasibility as it is a very cheap material that can be used in preliminary approaches during R&D phases or other applications. Indeed, the use of these types of 3D printers does not represent a huge investment, the purchase costs for the general public being under five hundred euros, making it possible to obtain an ABS chip with a manufacturing cost less than two euros per chip.

In the following, LNC D_{Hz} formulated with the Si/Glass chip for a given stock solution were called X_i, and those formulated with the same stock solution but the PEEK chip, Y_i.

Figure 7 gathers results (D_{Hz} and PDI) obtained with the PEEK and the Si/Glass chips and are represented by violin plots: considering confidence intervals, there is no significant difference between both chips. A complementary Passing-Bablok regression study confirmed this assessment (See SI Fig. S6-1), showing there is no proportional nor systematic error. This result is also comforted by a Bland-Altman analysis showing a good homogeneity and dispersion whatever targeted sizes (Fig. S6-2). All these studies statistically demonstrated that although the two chips were produced by different technologies, and despite the different channel sizes, formulated LNCs are not significantly different. It paves the road toward *in-situ* experiments using the Si/Glass chip with for example optical fiber dynamic light scattering in the laboratory, SAXS or small-angle neutron scattering on large facilities. On the other hand, the PEEK chip can be used to formulate LNCs for R&D tests and production of nanoparticulate enabled medicinal products.

In the perspective of a "scaled-up" production, besides an obvious multiple chip parallelization, it would be interesting to investigate a nominal flowrate increase in this PEEK chip. In this way, the same statistical approach was carried out using a fivefold increased flowrate (2.1 mL/min for the lowest and 10.5 mL/min for the highest). Going further could damage the chip and trigger leaks. Violin plots, Passing-Bablok and Bland-Altman analyses show a small systematic decrease of size when increasing the flow rate, but this drop (below 5% for biggest LNCs) stays perfectly reasonable (see SI section S6: Fig. S6-3 to S6-5).

After the formulation of all the different LNCs, pressure limit tests have been carried out. They revealed an admissible pressure of about 42 bar. Besides, this maximum allowable pressure was not due to the chip by itself but to the maximum allowable pressure for the connectors. With a different system, the maximum pressure mentioned in the literature for a 3D printed chip and connector was about 7 bar (71). In that study with the Galechip pilot, the pressure conveyed to the liquid was limited to 8 bar. The measured pression at high flow rate, without configuration changes, were around 2.9 bar for the water line and 1.5 bar for the oil line. In these conditions, the PEEK chips have been intensively used (10 hours a day, 5 days a week) over a year and half to produce LNC. An increase of the flowrate up to 27.5 mL/min without any change on the fluidic environment seemed thus possible (capillaries, back-pressure regulators, flowmeters). Finally, one trial was conducted allowing to reach 30 mL/min without any damage (data not shown).

3.3. SAXS Results

SAXS intensity curves from well-known LNC-PIC samples (an LNC 25 nm PIC batch suspension diluted at 1% w/w) were collected from classical glass-borosilicate capillaries with 1.5 mm diameter and 10 µm thick walls. Figure 8 shows the absolute scale intensity curves obtained after data treatment and the corresponding best fits to the data. The SAXS intensity curves, plotted as a function of the scattering vector Q (in $Å^{-1}$), were obtained applying the standard beam-line corrections (72) to reach an absolute scale (in cm^{-1} units) based on the measurement of the reference scattering intensity of pure water (for further details, see the corresponding SI section Fig. S7-1, S7-2 and Table S7-1). The water filled capillary reference signal (grey symbols and curve in cm^{-1} units) is shown in Figure 8 and in Figure S7-1A.

In order to compare the SAXS signal from diluted LNC suspensions measured in the microfluidic chip and in classical capillaries, the same suspension was measured in both environments at rest. The microfluidic chip was totally filled with the suspension used previously, and measurements were carried out through the microfluidic chip in the channel section accessible after the Y junction. The absolute scale SAXS signal is plotted in Figure 8 (cyan symbols and line) and it is identical to the one measured within capillaries in the low Q range (plotted with red symbols and curve). For diluted samples, air and instrument window scattering contributions dominate all the raw data intensity curves at smaller Q measured values. On the contrary, the large Q range shows a slightly higher intensity due to an increase of the cell wall contribution and solvent scattering amount in comparison with the measurements carried out with capillaries. Nevertheless, the same trend appears for the raw signal measured within the microfluidic chip filled with pure water (see Fig. S7-1B), so that after subtraction of all these contributions (air, instrument windows scattering, sample holder and solvent scattering), the LNC SAXS curve measured with the microfluidic chip is identical to the one measured in the capillary. It is noteworthy that for these settings, diluted LNC suspensions at 1% (w/w) gave the same SAXS intensity in absolute scale units and error bars amplitude in a capillary as in the microfluidic channel.

The diluted LNC SAXS data were also fitted over the full Q range (0.01 to 0.25 $Å^{-1}$, Figure S7-1 black curves over red symbols). The model used to fit the data in absolute scale (73) is based on a log-normal distribution of spherical particles with a core-shell structure form factor (74) and a hard sphere model for inter particles interactions using the Percus-Yevick closure structure factor (75). Excellent fits were obtained with a fixed electron density for the solvent (0.334 $Å^{-3}$) and the resulting electron density profile is plotted in Fig. S7-2A. Fitted parameters and resulting quantities were all in excellent agreement with other experimental LNC determinations (calculated electron densities from pure materials are given in the SI, Table S7-1) and sample composition. The core electron density ($r_{e,C}$ = 0.310 $Å^{-3}$) and core radius (R_C = 10.3 ± 0.2 nm) correspond to a Labrafac oil core; the hybrid shell showed a higher electron density ($r_{e,S}$ = 0.432 $Å^{-3}$) as expected near the Labrafac/Kolliphor interface and a thickness

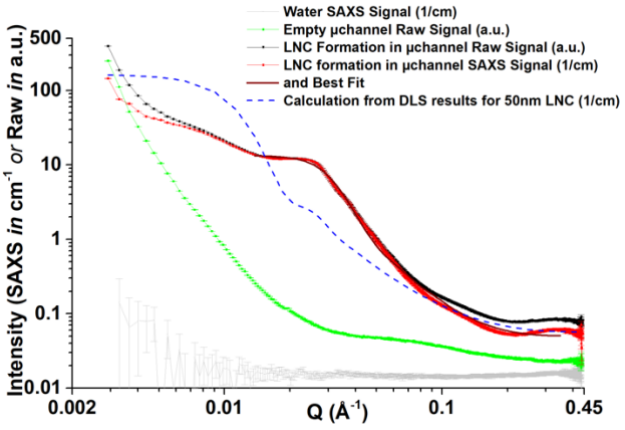

Fig 9: Raw signals and SAXS curve measurements carried out in the microfluidic channel under flow during formulation of LNCs 50 nm at 5% (w/w). The SAXS curve and its best fit are plotted with red dots and line and a brown line, respectively. Other color codes are identical to the ones used previously. The dashed line is the SAXS curve calculated for stable LNC core-shell particles (R_C=48.5 nm, PDI ~ 0.07 and same values as previously for other parameters).

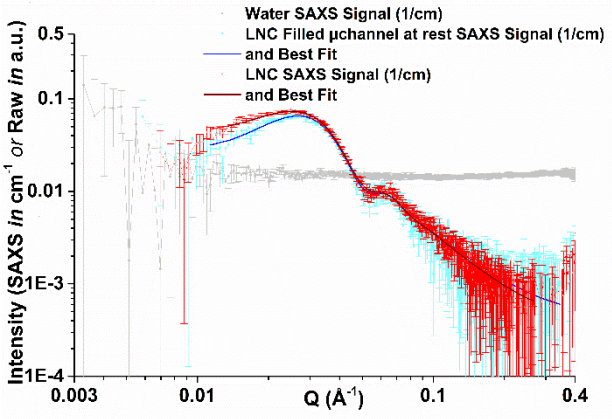

Fig 8: SAXS intensity (in absolute scale units, cm^{-1}) curves plotted as a function of the scattering vector on a log-log scale for measurements carried out within classical borosilicate glass capillaries (red dots) of the LNCs 25 nm suspension at 1% (w/w). The cyan dots correspond to the same suspension measured at rest in the microfluidic channel of the Si/Glass chip (4 mm away from the Y junction (see Fig. 4C). The best fits to the data are plotted on top of the two SAXS data curves in cm^{-1} and correspond to the wine-red and blue lines, respectively). The grey curve corresponds to measured pure water scattering (curve around 0.0168 cm^{-1}) and is plotted as a guide to the eyes. Raw data curves are shown in the SI (Fig S7-2).

of t_S = 1.2 ± 0.3 nm, leading to an average external diameter around 23 nm slighly smaller than D_{Hz} = 23.11 nm measured by DLS. But, as previously shown using a similar model for crew-cut micelles with hydrated PEGylated chains, highlly swollen PEO segments do not participate to the shell X-ray contrast and are hardly seen as their electron density is very close to the solvent one (73). The model, which also integrates the instrumental broadening, also fits the size distribution of the core radius and shell thickness in the form of a log-normal and a normal distribution respectivelly (see Fig. S7-2B). The standard deviation of the natural logarithm of the core size distribrution is s_c = 0.16 ± 0.03, i.e. equivalent to PDI = exp(s_c^2) - 1 = 0.026. The standard deviation of the shell thickness distribution is s_s = 0.12 ± 0.05. These results are in good agreement with the polydispersity obtained by DLS analysis (PDI = 0.064). These results validate our microfluidic chip design for SAXS experiments.

Data collected during the concomitant injection of water (1,000.0 µL/min) and oil plus surfactants (47.1 µL/min) are plotted in Figure 9 for a LNC 50 target formulation (48.3 ± 0.3 nm measured by DLS) at 5% w/w concentration in water. The raw signal curve (black symbole and curve) shows that the sample scattering measured at 4 mm from the Y junction is much higher than the empty chip scattering (green symbols and curve), except at very low angles (Q < 0.003 $Å^{-1}$) near the beam stop region. The simple model of core-shell LNC particles does not fit the low angle data where large scale scattering contributions appeared (below 10^{-2} $Å^{-1}$) and are not present when measuring stable LNC suspensions at rest. The large scale signal might come from residual intermediate phases that exist during the ongoing process of the water and oil phase mixing. Intermediate structures with such large scales are expected during an emulsion phase inversion mixing mechanism (62) . Among these, bicontineous phases or multiple emulsions could be responsible for such a SAXS signal but cannot be adressed unambigously to this point. Nevertheless, the data above 10^{-2} $Å^{-1}$ were tentatively fitted since the signal was quite stable in time. Data could be modeled by either: i) swollen inverse micelles (62) in the disappearing oil phase,

or ii) already formed smaller core-shell structures. Both fits were obtained with polydisperse ($s \sim 0.27$) spherical particles with a diameter from 8 to 10 nm and a scattering electron density contrast corresponding to a water/oil interface (0.027 $Å^{-3}$). Note that out of the microfluidic chip, stable LNCs with 48 nm diameter were obtained and their calculated SAXS curve has been plotted with a blue dashed line in Figure 9 for comparison. Few millimiters away form the Y junction intermediate phases of the owngoing emulsion phase inversion process were probed. They contain structures smaller than the 50 nm LNCs recovered at the end. The identification of intermediate phases along the flow, as a function of the flow rate, concentrations and temperatures, is far beyond the scope of the present paper. Moreover, stable LNCs could not be formulated after just a Y junction in absence of square turns so that the number and shape of the turns are also important parameters to be studied. This chip conceived for SAXS experiments is perfectly designed for that.

4. Conclusion

This paper demonstrated how additive manufacturing and microfabrication techniques were complementary in the development of the Galenic Lab-on-a-Chip concept for the characterization and the production of LNC nanomedicines. Chips have been manufactured thanks to two different technologies and successfully used for LNC formulations. 3D printing can be used to build microfluidic chip devices, heater housings and connectors.

Besides its considerably lower manufacturing costs and time in comparison to DRIE technologies, 3D printing suits particularly well to produce prototypes. First with ABS for its easiness of implementation and its reduced costs. Then with PEEK which is a better candidate for medical applications due to its capacity to endure autoclave cycles and gamma sterilization and its mechanical and chemical resistance to several aggressive solvents (like acetone, isopropyl alcohol and many other solvents) (76,77). PEEK is fully compliant with the good pharmaceutical practices in view of an industrial transposition and an easy scaling-up by the means multiple chip parallelization. Besides, it was also shown that Si/Glass chips designed for X-ray scattering experiments are unique *in-situ* tools to characterize formulations and process phenomenology. However, Si/Glass chips are still too expensive and time consuming to manufacture in the outlook of industrial production. SAXS analysis for well-known and stable LNC suspensions at rest confirmed DLS results, i.e. the LNC overall radius and size polydispersity, and brought additional information about the LNC composition and structure. Under flow and near the Y-junction of the mixer, the phenomenology was more complex, and X-rays revealed spatially inhomogeneous situations and intermediate liquid crystal phases with large scale structures as expected for an ongoing emulsion phase inversion process. This opens the field to further investigations of these intermediate states along the flow using smaller synchrotron X-Ray beams (below 20 µm in size). Furthermore, other experiments not presented in this paper validated the possibility to use the Si/Glass chip in small angle neutron scattering experiments. Despite the width of usual neutron beams, the scattering contrast of silicon walls with the solution can be matched by using an appropriate H_2O/D_2O mixture. As well, a good sensitivity to the core composition can be achieved once loaded with labelled drugs of interest.

Conflicts of interest

The authors want to mention that some of them (Calvignac B, Rolley N, Gimel J-C, Lefebvre G) are also authors of the patent cited (55).

Acknowledgements

This work has been carried out within the RESOLVE research project (ANR-17-CE24-0033) financially supported by EuroNanoMed-III (8th call) and the French ANR, the GALECHIP project supported by CNRS and ALDEV, the EcoNEL and Phy2miFor research projects supported by University of Angers. The authors thank the SCIAM laboratory (Angers, France) for characterizations of chips by opto-numerical microscopy and APIUM GmbH (Karlsruhe, Germany) for the technical support for 3D printing of PEEK.

The authors are grateful for the technical support from Maxime BELLANGER for its implication on microfluidic Lipid Nanocapsule formulation.

The authors thank gratefully Thomas GALLARD, Thomas CLEQUIN, Grégoire BOUGEARD for their implication on the design of the microfluidic connectors.

Notes and references

1. Majumder J, Taratula O, Minko T. Nanocarrier-based systems for targeted and site specific therapeutic delivery. Advanced Drug Delivery Reviews. 2019 Apr 1;144:57–77.

2. Pushpalatha R, Selvamuthukumar S, Kilimozhi D. Nanocarrier mediated combination drug delivery for chemotherapy – A review. Journal of Drug Delivery Science and Technology. 2017 Jun 1;39:362–71.

3. Kurmi BD, Patel P, Paliwal R, Paliwal SR. Molecular approaches for targeted drug delivery towards cancer: A concise review with respect to nanotechnology. Journal of Drug Delivery Science and Technology. 2020 Jun 1;57:101682.

4. Chen W, Zhou S, Ge L, Wu W, Jiang X. Translatable High Drug Loading Drug Delivery Systems Based on Biocompatible Polymer Nanocarriers. Biomacromolecules. 2018 Jun 11;19(6):1732–45.

5. Chariou PL, Ortega-Rivera OA, Steinmetz NF. Nanocarriers for the Delivery of Medical, Veterinary, and Agricultural Active Ingredients. ACS Nano. 2020 Mar 24;14(3):2678–701.

6. Farjadian F, Ghasemi A, Gohari O, Roointan A, Karimi M, Hamblin MR. Nanopharmaceuticals and nanomedicines currently on the market: challenges and opportunities. Nanomedicine. 2018 Nov 19;14(1):93–126.

7. Barauskas J, Cervin C, Jankunec M, Špandyreva M, Ribokaitė K, Tiberg F, et al. Interactions of lipid-based liquid crystalline nanoparticles with model and cell membranes. International Journal of Pharmaceutics. 2010 May 31;391(1):284–91.

8. Murgia S, Falchi AM, Mano M, Lampis S, Angius R, Carnerup AM, et al. Nanoparticles from Lipid-Based Liquid Crystals: Emulsifier Influence on Morphology and Cytotoxicity. J Phys Chem B. 2010 Mar 18;114(10):3518–25.

9. Hinton TM, Grusche F, Acharya D, Shukla R, Bansal V, Waddington LJ, et al. Bicontinuous cubic phase nanoparticle lipid chemistry affects toxicity in cultured cells. Toxicol Res. 2013 Dec 5;3(1):11–22.

10. Huynh NT, Passirani C, Saulnier P, Benoit JP. Lipid nanocapsules: A new platform for nanomedicine. International Journal of Pharmaceutics. 2009 Sep 11;379(2):201–9.

11. Matougui N, Boge L, Groo A-C, Umerska A, Ringstad L, Bysell H, et al. Lipid-based nanoformulations for peptide delivery. International Journal of Pharmaceutics. 2016 Apr 11;502(1):80–97.

12. Niu Z, Conejos-Sánchez I, Griffin BT, O'Driscoll CM, Alonso MJ. Lipid-based nanocarriers for oral peptide delivery. Advanced Drug Delivery Reviews. 2016 Nov 15;106:337–54.

13. Moura RP, Pacheco C, Pêgo AP, des Rieux A, Sarmento B. Lipid nanocapsules to enhance drug bioavailability to the central nervous system. Journal of Controlled Release. 2020 Jun 10;322:390–400.

14. Caputo F, Clogston J, Calzolai L, Rösslein M, Prina-Mello A. Measuring particle size distribution of nanoparticle enabled medicinal products, the joint view of EUNCL and NCI-NCL. A step by step approach combining orthogonal measurements with increasing complexity. Journal of Controlled Release. 2019 Apr 10;299:31–43.

15. Djuris J, Djuric Z. Modeling in the quality by design environment: Regulatory requirements and recommendations for design space and control strategy appointment. International Journal of Pharmaceutics. 2017 Nov 30;533(2):346–56.

16. Bastogne T. Quality-by-design of nanopharmaceuticals – a state of the art. Nanomedicine: Nanotechnology, Biology and Medicine. 2017 Oct 1;13(7):2151–7.

17. Li J, Qiao Y, Wu Z. Nanosystem trends in drug delivery using quality-by-design concept. Journal of Controlled Release. 2017 Jun 28;256:9–18.

18. Heurtault B, Saulnier P, Pech B, Proust J-E, Benoit J-P. A Novel Phase Inversion-Based Process for the Preparation of Lipid Nanocarriers. Pharm Res. 2002 Jun 1;19(6):875–80.

19. Hureaux J, Lagarce F, Gagnadoux F, Clavreul A, Benoit J-P, Urban T. The adaptation of lipid nanocapsule formulations for blood administration in animals. International Journal of Pharmaceutics. 2009 Sep 11;379(2):266–9.

20. Roger E, Lagarce F, Benoit J-P. Development and characterization of a novel lipid nanocapsule formulation of Sn38 for oral administration. European Journal of Pharmaceutics and Biopharmaceutics. 2011 Sep 1;79(1):181–8.

21. Groo A-C, Saulnier P, Gimel J-C, Gravier J, Ailhas C, Benoit J-P, et al. Fate of paclitaxel lipid nanocapsules in intestinal mucus in view of their oral delivery. Int J Nanomedicine. 2013;8:4291–302.

22. Briot T, Roger E, Lautram N, Verger A, Clavreul A, Lagarce F. Development and in vitro evaluations of new decitabine nanocarriers for the treatment of acute myeloid leukemia. International Journal of Nanomedicine. 2017 Nov 23;

23. Ramadan A, Lagarce F, Tessier-Marteau A, Thomas O, Legras P, Macchi L, et al. Oral fondaparinux: use of lipid nanocapsules as nanocarriers and in vivo pharmacokinetic study. Int J Nanomedicine. 2011;6:2941–51.

24. Hirsjärvi S, Qiao Y, Royere A, Bibette J, Benoit J-P. Layer-by-layer surface modification of lipid

nanocapsules. European Journal of Pharmaceutics and Biopharmaceutics. 2010 Oct 1;76(2):200–7.

25. Danhier F, Messaoudi K, Lemaire L, Benoit J-P, Lagarce F. Combined anti-Galectin-1 and anti-EGFR siRNA-loaded chitosan-lipid nanocapsules decrease temozolomide resistance in glioblastoma: In vivo evaluation. International Journal of Pharmaceutics. 2015 Mar 15;481(1):154–61.

26. Anton N, Vandamme TF. The universality of low-energy nano-emulsification. International Journal of Pharmaceutics. 2009 Jul 30;377(1):142–7.

27. Valencia PM, Farokhzad OC, Karnik R, Langer R. Microfluidic technologies for accelerating the clinical translation of nanoparticles. Nature Nanotechnology. 2012 Oct 1;7(10):623–9.

28. Grossman JH, McNeil SE. Nanotechnology in cancer medicine. Physics today. 2012;65(8):38.

29. Liu D, Zhang H, Fontana F, Hirvonen JT, Santos HA. Current developments and applications of microfluidic technology toward clinical translation of nanomedicines. Advanced Drug Delivery Reviews. 2018 Mar 15;128:54–83.

30. Garg S, Heuck G, Ip S, Ramsay E. Microfluidics: a transformational tool for nanomedicine development and production. Journal of Drug Targeting. 2016 Oct 20;24(9):821–35.

31. Khan IU, Serra CA, Anton N, Vandamme TF. Production of nanoparticle drug delivery systems with microfluidics tools. Expert Opinion on Drug Delivery. 2015 Apr 3;12(4):547–62.

32. Martins P, Rosa D, Baptista ARF and PV. Nanoparticle Drug Delivery Systems: Recent Patents and Applications in Nanomedicine. Recent Patents on Nanomedicine (Discontinued). 2013 Sep 30;

33. Lim J-M, Karnik R. Optimizing the discovery and clinical translation of nanoparticles: could microfluidics hold the key? Nanomedicine. 2014 Jun 1;9(8):1113–6.

34. Ran R, Sun Q, Baby T, Wibowo D, Middelberg APJ, Zhao C-X. Multiphase microfluidic synthesis of micro- and nanostructures for pharmaceutical applications. Chemical Engineering Science. 2017 Sep 21;169:78–96.

35. Ma Q, Cao J, Gao Y, Han S, Liang Y, Zhang T, et al. Microfluidic-mediated nano-drug delivery systems: from fundamentals to fabrication for advanced therapeutic applications. Nanoscale. 2020;12(29):15512–27.

36. Kimura N, Maeki M, Sasaki K, Sato Y, Ishida A, Tani H, et al. Three-dimensional, symmetrically assembled microfluidic device for lipid nanoparticle production. RSC Adv. 2021;11(3):1430–9.

37. Serra CA, Chang Z. Microfluidic-Assisted Synthesis of Polymer Particles. Chemical Engineering & Technology. 2008 Aug 1;31(8):1099–115.

38. Jeong WJ, Kim JY, Choo J, Lee EK, Han CS, Beebe DJ, et al. Continuous Fabrication of Biocatalyst Immobilized Microparticles Using Photopolymerization and Immiscible Liquids in Microfluidic Systems. Langmuir. 2005 Apr 1;21(9):3738–41.

39. Mizuno M, Toyota T, Konishi M, Kageyama Y, Yamada M, Seki M. Formation of Monodisperse Hierarchical Lipid Particles Utilizing Microfluidic Droplets in a Nonequilibrium State. Langmuir. 2015 Mar 3;31(8):2334–41.

40. van Swaay D, deMello A. Microfluidic methods for forming liposomes. Lab Chip. 2013;13(5):752–67.

41. Maeki M, Kimura N, Sato Y, Harashima H, Tokeshi M. Advances in microfluidics for lipid nanoparticles and extracellular vesicles and applications in drug delivery systems. Advanced Drug Delivery Reviews. 2018;128:84–100.

42. Suryawanshi PL, Gumfekar SP, Bhanvase BA, Sonawane SH, Pimplapure MS. A review on microreactors: Reactor fabrication, design, and cutting-edge applications. Chemical Engineering Science. 2018 Nov 2;189:431–48.

43. Chastek TQ, Beers KL, Amis EJ. Miniaturized dynamic light scattering instrumentation for use in microfluidic applications. Review of Scientific Instruments. 2007 Jul 1;78(7):072201.

44. Teh S-Y, Lin R, Hung L-H, Lee AP. Droplet microfluidics. Lab Chip. 2008 Jan 29;8(2):198–220.

45. Lee C-Y, Chang C-L, Wang Y-N, Fu L-M. Microfluidic Mixing: A Review. Int J Mol Sci. 2011 May 18;12(5):3263–87.

46. Zhu P, Wang L. Passive and active droplet generation with microfluidics: a review. Lab Chip. 2016 Dec 20;17(1):34–75.

47. Nguyen N-T, Wu Z. Micromixers—a review. J Micromech Microeng. 2004 Dec;15(2):R1–16.

48. Cai G, Xue L, Zhang H, Lin J. A Review on Micromixers. Micromachines. 2017 Sep;8(9):274.

49. Beuvier T, Panduro EAC, Kwaśniewski P, Marre S, Lecoutre C, Garrabos Y, et al. Implementation of in situ SAXS/WAXS characterization into silicon/glass microreactors. Lab Chip. 2015 Apr 21;15(9):2002–8.

50. Santana HS, Palma MSA, Lopes MGM, Souza J, Lima GAS, Taranto OP, et al. Microfluidic Devices and 3D Printing for Synthesis and Screening of Drugs and Tissue Engineering. Ind Eng Chem Res. 2020 Mar 4;59(9):3794–810.

51. Naderi A, Bhattacharjee N, Folch A. Digital Manufacturing for Microfluidics. Annual Review of Biomedical Engineering. 2019;21(1):325–64.

52. Tiboni M, Benedetti S, Skouras A, Curzi G, Perinelli DR, Palmieri GF, et al. 3D-printed microfluidic chip for the preparation of glycyrrhetinic acid-loaded ethanolic liposomes. International Journal of Pharmaceutics. 2020 Jun 30;584:119436.

53. Chang Y, Jiang J, Chen W, Yang W, Chen L, Chen P, et al. Biomimetic metal-organic nanoparticles prepared with a 3D-printed microfluidic device as a novel formulation for disulfiram-based therapy against breast cancer. Applied Materials Today. 2020 Mar 1;18:100492.

54. Tiboni M, Tiboni M, Pierro A, Del Papa M, Sparaventi S, Cespi M, et al. Microfluidics for nanomedicines manufacturing: An affordable and low-cost 3D printing approach. International Journal of Pharmaceutics. 2021 Apr 15;599:120464.

55. Calvignac B, Rolley N, Bastiat G, Gimel J-C, Roger E, Lefebvre G, et al. Procédé continu de nano-émulsification par inversion de phase en concentration. Angers; FR1908392, 2019.

56. Balzeau J, Pinier M, Berges R, Saulnier P, Benoit J-P, Eyer J. The effect of functionalizing lipid nanocapsules with NFL-TBS.40-63 peptide on their uptake by glioblastoma cells. Biomaterials. 2013 Apr 1;34(13):3381–9.

57. Bastiancich C, Lemaire L, Bianco J, Franconi F, Danhier F, Préat V, et al. Evaluation of lauroyl-gemcitabine-loaded hydrogel efficacy in glioblastoma rat models. Nanomedicine. 2018 Aug 1;13(16):1999–2013.

58. Laermer F, Franssila S, Sainiemi L, Kolari K. Chapter 21 - Deep Reactive Ion Etching. In: Tilli M, Motooka T, Airaksinen V-M, Franssila S, Paulasto-Kröckel M, Lindroos V, editors. Handbook of Silicon Based MEMS Materials and Technologies (Second Edition). Boston: William Andrew Publishing; 2015. p. 444–69. (Micro and Nano Technologies).

59. Laermer F, Schilp A. Method of anisotropically etching silicon. US5501893A, 1996.

60. Althaus J, Padeste C, Köser J, Pieles U, Peters K, Müller B. Nanostructuring polyetheretherketone for medical implants. European Journal of Nanomedicine. 2012;4(1):7–15.

61. Lefebvre G, Riou J, Bastiat G, Roger E, Frombach K, Gimel J-C, et al. Spontaneous nano-emulsification: Process optimization and modeling for the prediction of the nanoemulsion's size and polydispersity. International Journal of Pharmaceutics. 2017;534(1):220–8.

62. Komaiko J, Mcclements D. Formation of Food-Grade Nanoemulsions Using Low-Energy Preparation Methods: A Review of Available Methods. Comprehensive Reviews in Food Science and Food Safety. 2016;15:n/a-n/a.

63. Solans C, Sole I. Nano-emulsions: Formation by low-energy methods. Current Opinion in Colloid & Interface Science. 2012 Oct 1;17:246–54.

64. Koppel DE. Analysis of Macromolecular Polydispersity in Intensity Correlation Spectroscopy: The Method of Cumulants. J Chem Phys. 1972 Dec 1;57(11):4814–20.

65. Passing H., Bablok W. A New Biometrical Procedure for Testing the Equality of Measurements from Two Different Analytical Methods. Application of linear regression procedures for method comparison studies in Clinical Chemistry, Part I. cclm. 2009;21(11):709.

66. Bland JM, Altman D. Statistical methods for assessing agreement between two methods of clinical measurement. The Lancet. 1986;327(8476):307–10.

67. Song H, Tice JD, Ismagilov RF. A Microfluidic System for Controlling Reaction Networks in Time. Angewandte Chemie International Edition. 2003;42(7):768–72.

68. Test de l'Alfawise U20 : tout ce qu'il faut savoir sur l'imprimante 3D [Internet]. All3DP. [cited 2019 Dec 2]. Available from: https://all3dp.com/fr/1/alfawise-u20-impimante-3d-test-avis/

69. Guttoff M, Saberi AH, McClements DJ. Formation of vitamin D nanoemulsion-based delivery systems by spontaneous emulsification: Factors affecting particle size and stability. Food Chemistry. 2015 Mar 15;171:117–22.

70. Abstiens K, Goepferich AM. Microfluidic manufacturing improves polydispersity of multicomponent polymeric nanoparticles. Journal of Drug Delivery Science and Technology. 2019 Feb 1;49:433–9.

71. van den Driesche S, Lucklum F, Bunge F, Vellekoop MJ. 3D Printing Solutions for Microfluidic Chip-To-World Connections. Micromachines (Basel). 2018 Feb 6;9(2).

72. SWING | Centre de rayonnement synchrotron français [Internet]. [cited 2020 May 4]. Available from: https://www.synchrotron-soleil.fr/fr/lignes-de-lumiere/swing

73. Soni SS, Brotons G, Bellour M, Narayanan T, Gibaud A. Quantitative SAXS Analysis of the P123/Water/Ethanol Ternary Phase Diagram. J Phys Chem B. 2006 Aug 1;110(31):15157–65.

74. Guinier A, Fournet G. Small-angle scattering of X-rays. John Wiley and Sons. New-York; 1955. 288 p.

75. Percus JK, Yevick GJ. Analysis of Classical Statistical Mechanics by Means of Collective Coordinates. Phys Rev. 1958 Apr 1;110(1):1–13.

76. Cogswell FN. Thermoplastic aromatic polymer composites. 1st ed. Oxford: Butterworth–Heinemann; 1993. 277 p.

77. Schweitzer PA. Mechanical and Corrosion-Resistant Properties of Plastics and Elastomers [Internet]. 2000 [cited 2020 Jun 15]. Available from: /paper/Mechanical-and-Corrosion-Resistant-Properties-of-Schweitzer/acfd2231a2be8501c8f620ce6af125c82a4945ef

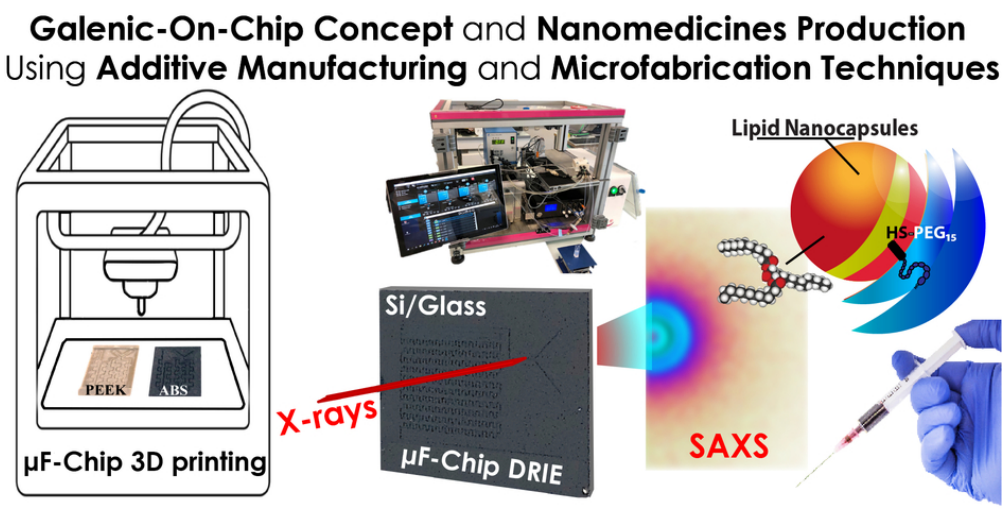

79x39mm (300 x 300 DPI)

Galenic Lab-On-Chip Concept and Nanomedicines Production Using Additive Manufacturing and Microfabrication Techniques

Nicolas ROLLEY[a], Marie BONNIN[a], Guillaume LEFEBVRE[a], Sylvain VERRON[b], Sylwester BARGIEL[c], Laurent ROBERT[c], Jérémie RIOU[a], Carl SIMONSSON[a], Thomas BIZIEN[d], Jean-Christophe GIMEL[a], Jean-Pierre BENOIT[a], Guillaume BROTONS[e], Brice CALVIGNAC[a]

Supporting Information

S1 Galechip pilot

Figure S1-1 and Figure S1-2 present the main elements of the home-made Galechip pilot.

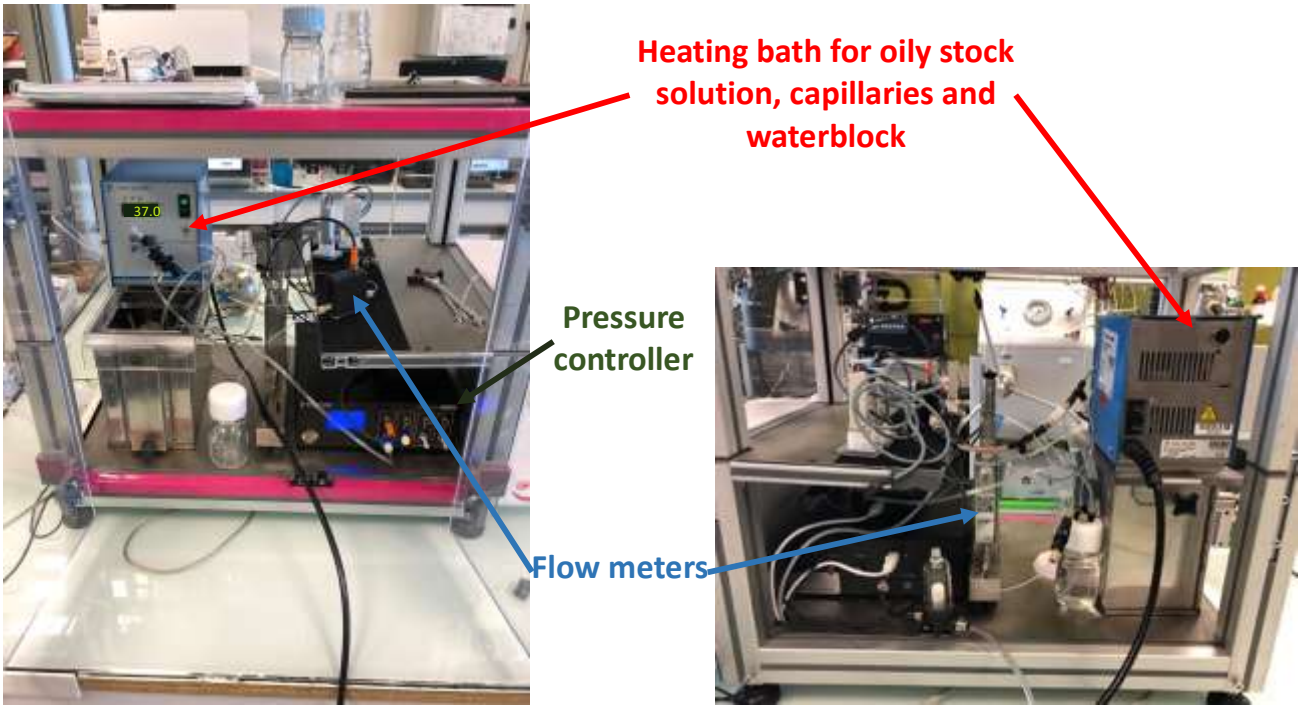

Figure S1-1: Global overview of the Galechip Pilot

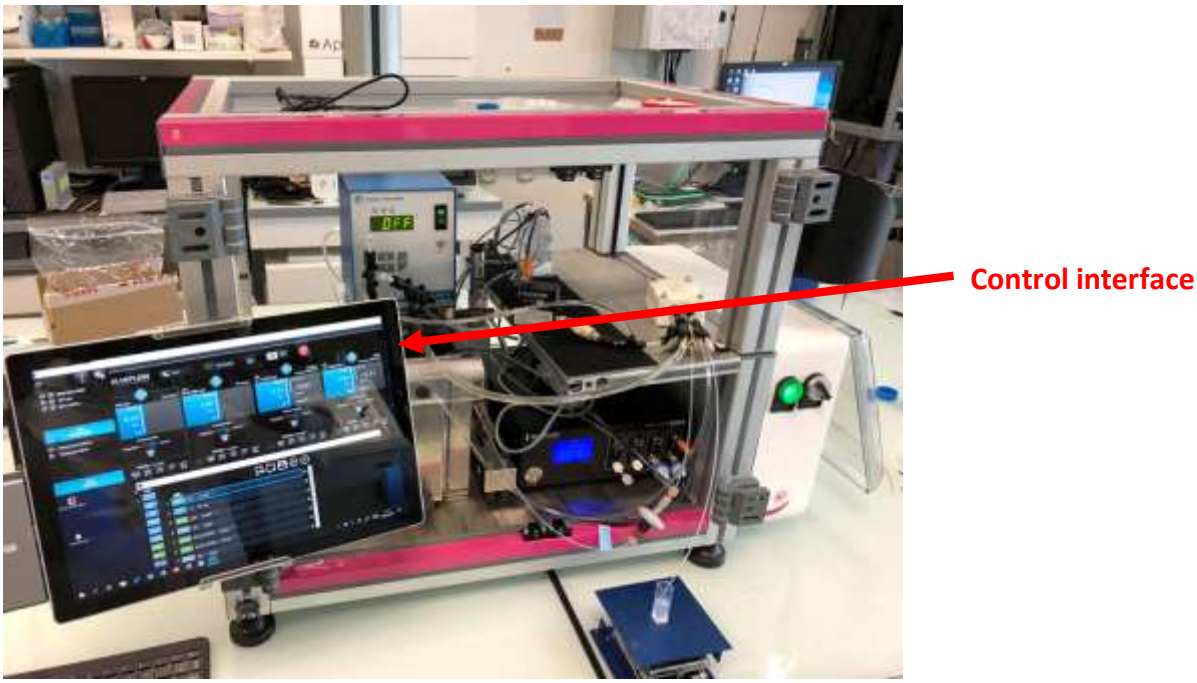

Figure S1-2: Galechip pilot for Lipid Nanocapsule production

S2 Chips design

The additive manufacturing of ABS (Verbatim Gmbh, Eschborn, Germany) and PEEK (Apium Additive Technologies Gmbh, Karlsruhe, Germany) chips require four steps (Figure S2-1):

(A) The 3D chip design was modelled with a CAD software at the same dimensions as the Si/Glass chip, except for the channel section because of the limited resolution of the 3D printer. This led to a shorter channel length and less elbows. However, the fluid volume of the 3D printed chip was similar. All specifications of 3D printed chips are summarized in Table S2-1 in parallel with those of the Si/Glass chips.

(B) A slicing step, carried out with Simplify3D v4.1.1 (Cincinnati, USA), turns the 3D model into 2D slices to be processed by the printer. To avoid the warping phenomena during the printing (a classical 3D printing issue caused by the shrinkage of corners that leave the build plate during the printing, deforming the all printed object), twelve retaining support ribs were added around the chip (three on each side of the chip, located on critical locations, see Fig. 2B).

(C) The 3D printing of polymer microfluidic chips was carried out with the FDM technology using a P220 3D printer (Apium Additive Technologies Gmbh, Karlsruhe, Germany) for PEEK and a U20 3D Printer (Alfawise, Shenzhen, China) for ABS. The P220 3D printer was used with a 0.4 mm diameter nozzle at 480°C to extrude a 1.75 mm diameter PEEK filament. The fused filament was deposited on a 205 × 155 mm thermalized bed kept at 130°C. The U20 3D printer was used with a 0.4 mm diameter nozzle at 245°C to extrude a 1.75 mm diameter ABS filament. The fused filament was deposited on a 300 x 300 mm thermalized bed kept at 93°C.

(D) To obtain a functional chip, a machining step was needed. Retaining ribs were removed, and the chip surface was sanded. A FF230 milling machine (Proxxon SA, Wecker, Luxembourg) was used to drill 300 µm holes. The last step consisted in smoothing horizontal surfaces to eliminate potential leaks once the chip is integrated in the plugging device due to a surface rugosity.

Table S2-1 presents the targeted geometrical characteristics of the three used chips. The chip external sizes are similar so that they can be used with the same connectors and waterblock, but channel widths are different due to the limited resolution of 3D printers, resulting in a shorter total length but similar filling volume.

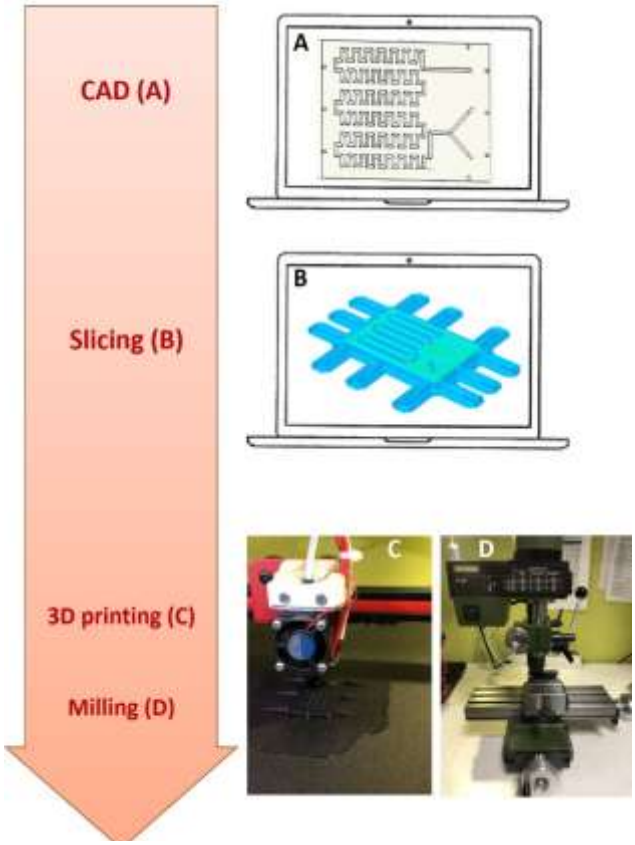

Fig S2-1: Flowchart for the chips manufacturing process. (A) CAD drawing. (B) Slicing of the CAD Drawing. (C) Printing of the chip (The Alfawise® 3D Printer used for the ABS printing is depicted on the picture). (D) Milling of the chip. (See section S2 for details)

Table S2-1: Geometrical characteristics of Si/Glass chip and 3D printed chips (ABS and PEEK)

	Si/Glass Chip	**ABS and PEEK 3D printed Chips**
Shape	Rectangle	Rectangle
Length	40 mm	40 mm
Width	26 mm	26 mm
Thickness	2.3 mm	2.6 mm
Channel design	"Y" junction (2 inlets and 1 outlet) with a 90° angle	"Y" junction (2 inlets and 1 outlet) with a 90° angle
Channel section	Rectangular: 300 x 1,500 µm	Rectangular: 600 x 1,500 µm
Mixing section	607 elbows with 90° angles	172 elbows with 90° angles
Channels total length	500 mm (including 453.46 mm from mixing point)	334.04 mm (including 318.65 mm from mixing point)

S3 Chip Plugging and heating devices manufactured by 3D printing

The water circulation chamber was covered with an aluminum heat-conducting plate to optimize heat transfers between the circulating water and the chip (Fig. 3B in the article). The fluidic connectors (part (2) in Fig. 3A and 3B in the article) were composed of two inlets and one outlet which were tapped in 10/32 to connect capillaries and sealed with o-rings (Fig. S3-1). Each channel was drilled with a Ø 400 µm hole. An L-shaped window was designed on the waterblock and the connector part to enable the X-Ray beam path (part (3) on Fig. 3C in the article). This L-shaped window coincided with the Y injection and many elbows of the integrated chip (zoom on Fig. 3C – more information on the SAXS implementation in section 2.5.2 SAXS analysis in the article). The waterblock and the connector part were designed using a CAD drawer and prototyped with the OBJET30 3D inkjet printer (Stratasys, Eden Prairie, USA). The 3D printing material used for both parts was the VeroWhitePlus RGD835 (Stratasys, Eden Prairie, USA) which was processed at a temperature below 48°C. Plugging and heating devices have been printed with 3D inkjet printing technology to ensure a good printing resolution of the seal groove, and of fluidic channels between plugs and chip.
Figure S3-1 shows the different parts of the waterblock device presented in section 2.3 in the article.

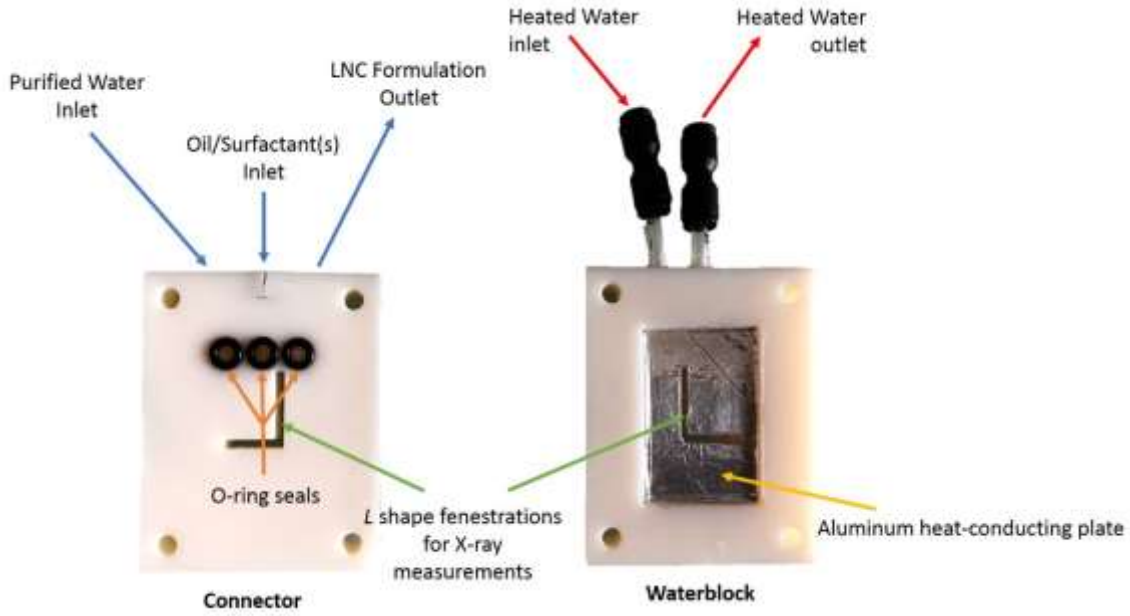

Figure S3-1: Details of the "all-in-one" plugging and heating device parts

S4 Digital microscopy on the different chips for channel characteristic measurements

Digital microscopy has been performed on the Si/Glass, ABS and PEEK chips. The results are presented in the main text (section 3.1.2 and Fig. 6). The following figures complete these results, presenting the measurement performed in each of the five regions of interest (ROI) for four different chips:

- A Si/Glass chip with its glass cover (Figure S4-1)
- A Si/Glass chip without glass cover (to confirm that the glass cover does not impact measurements): only one point is shown here and the chip design is different but repeatability of the DRIE process has been controlled on different design – data not shown) (Figure S4-2)
- An ABS chip (Figure S4-3)
- A PEEK chip (Figure S4-4)

Reproducibility of the fabrication processes (DRIE and 3D printing) have been controlled by doing the same measurements on different chips (data not shown).

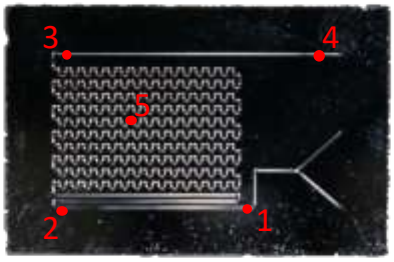

ROI 5	Channel 1	Channel 2	Channel 3	Channel 4	Channel 5
Length (µm)	1,421.89	1,434.11	1,436.99	1,439.65	1,438.89
Width (µm)	280.14	269.85	270.12	271.65	265.10
Angle (Deg) (L / R)	92.63 / 88.21	89.25 / 91.09	93.62 / 86.90	92.08 / 88.26	89.99 / 90.77

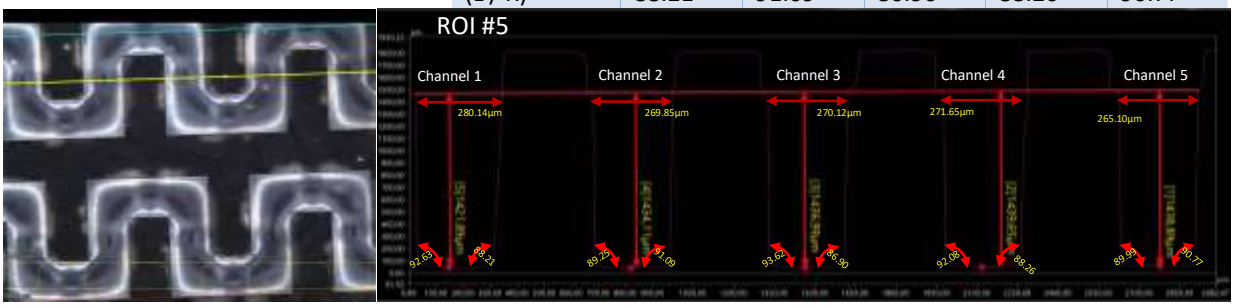

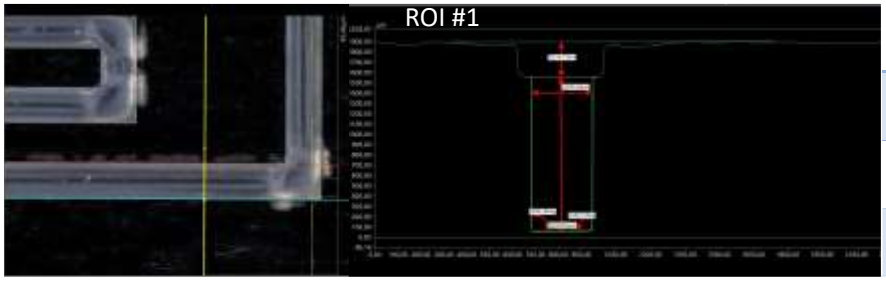

ROI 1	Channel 1
Length (µm)	1,498.10
Width (µm)	251.64
Angle (Deg) (L / R)	89.70 / 90.73

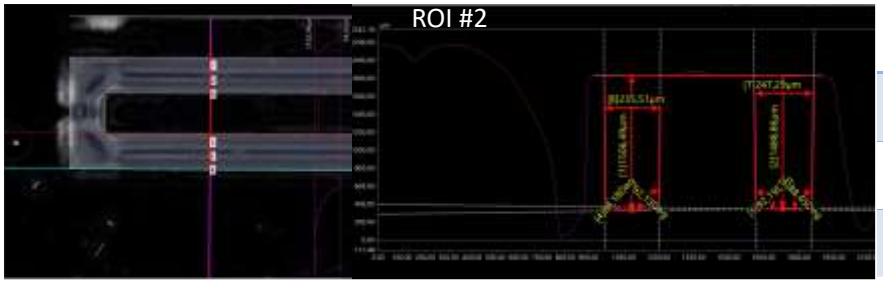

ROI 2	Channel 1	Channel 2
Length (µm)	1,506.49	1,488.86
Width (µm)	235.51	247.29
Angle (Deg) (L / R)	88.18 / 92.13	92.19 / 88.45

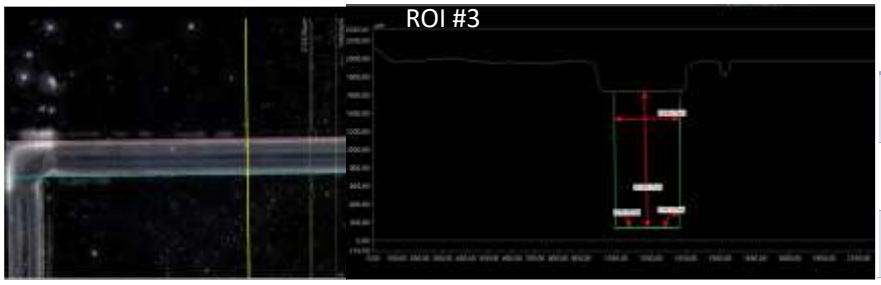

ROI 3	Channel 1
Length (µm)	1,501.74
Width (µm)	265.70
Angle (Deg) (L / R)	90.69 / 90.12

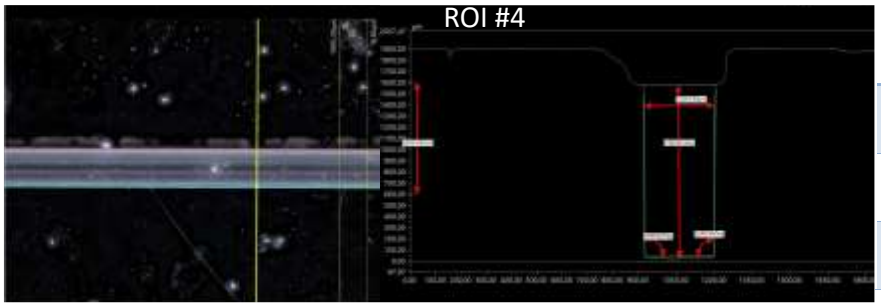

ROI 4	Channel 1
Length (µm)	1,546.72
Width (µm)	262.96
Angle (Deg) (L / R)	89.85 / 90.94

Figure S4-1: Digital microscopy observations of the Si/Glass chip with its glass cover: whole chip (including the localization of the 5 ROI) and zoom on each of the ROI, completed with the software measurement windows and tables with the obtained values.

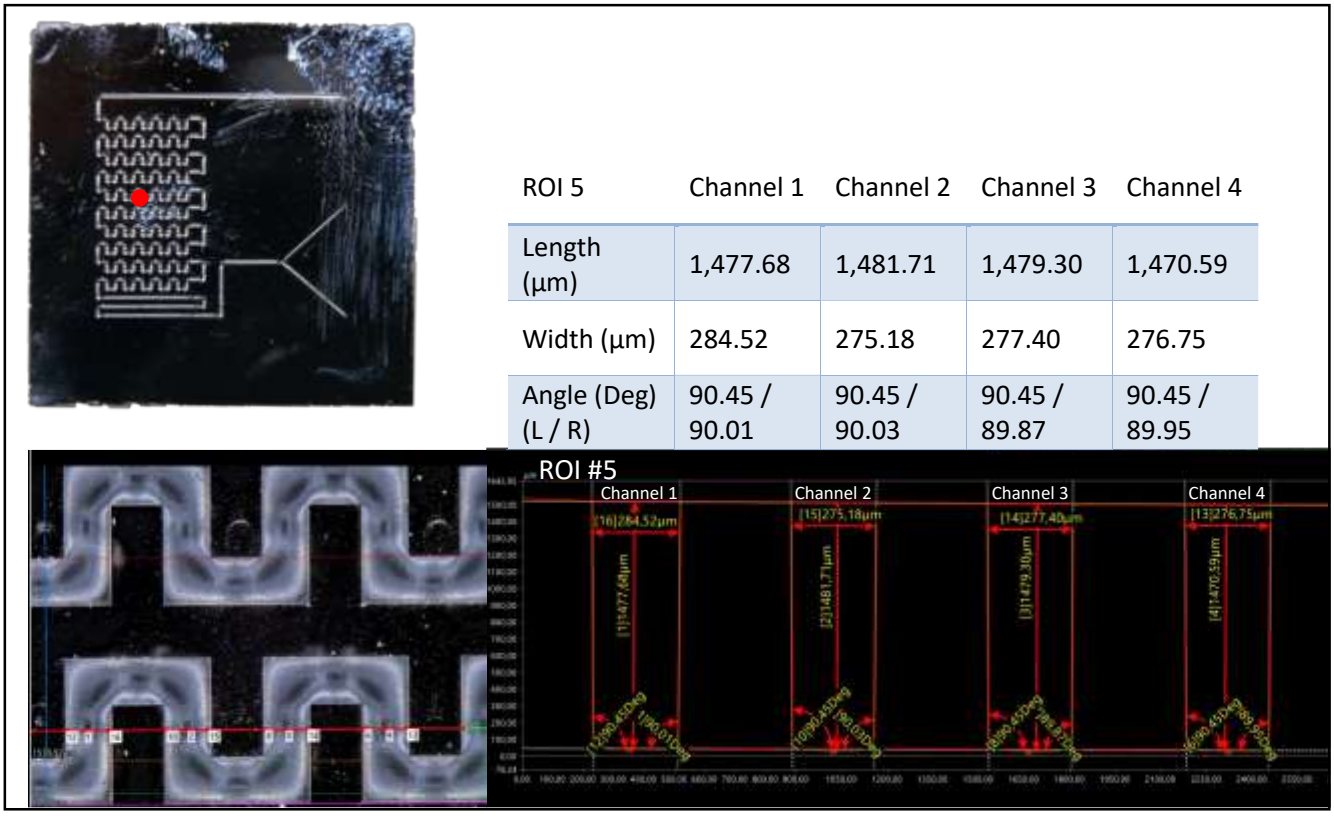

ROI 5	Channel 1	Channel 2	Channel 3	Channel 4
Length (µm)	1,477.68	1,481.71	1,479.30	1,470.59
Width (µm)	284.52	275.18	277.40	276.75
Angle (Deg) (L / R)	90.45 / 90.01	90.45 / 90.03	90.45 / 89.87	90.45 / 89.95

Figure S4-2: Digital microscopy observations of the Si/Glass chip without its glass cover: whole chip (including the localization of the ROI 5) and zoom on this ROI, completed with the software measurement windows and table with the obtained values.

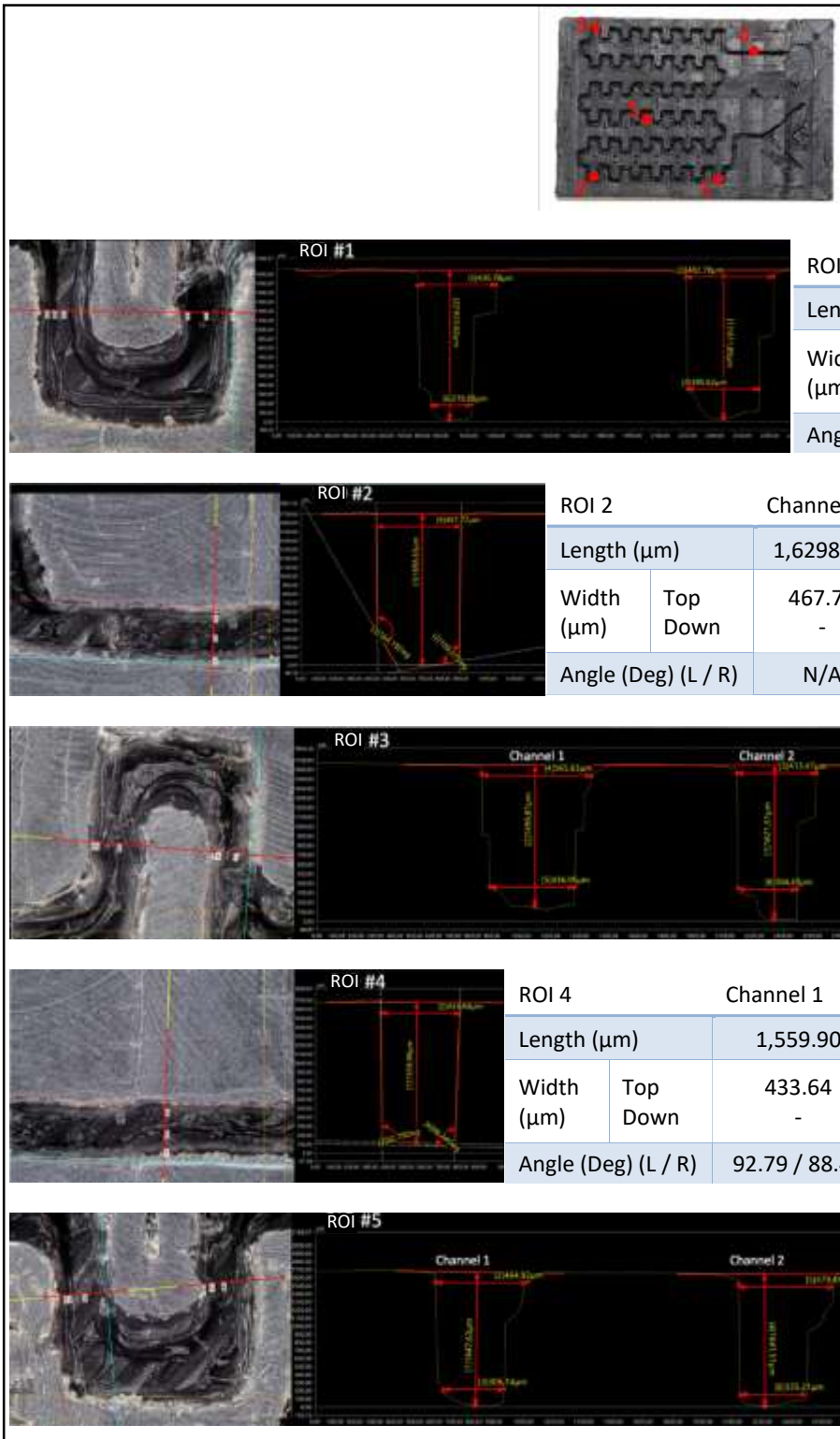

ROI 1		Channel 1	Channel 2
Length (µm)		1,623.62	1,611.89
Width (µm)	Top	430.78	482.78
	Down	218.88	390.62
Angle (Deg) (L / R)		N/A	N/A

ROI 2		Channel 1
Length (µm)		1,6298.63
Width (µm)	Top	467.72
	Down	-
Angle (Deg) (L / R)		N/A

ROI 3		Channel 1	Channel 2
Length (µm)		1,496.81	1,621.51
Width (µm)	Top	565.63	413.47
	Down	436.95	304.43
Angle (Deg) (L / R)		N/A	N/A

ROI 4		Channel 1
Length (µm)		1,559.90
Width (µm)	Top	433.64
	Down	-
Angle (Deg) (L / R)		92.79 / 88.44

ROI 5		Channel 1	Channel 2
Length (µm)		1,647.63	1,641.51
Width (µm)	Top	464.92	479.49
	Down	306.14	335.21
Angle (Deg) (L / R)		N/A	N/A

Figure S4-3: Digital microscopy observations of the ABS chip: whole chip (including the localization of the 5 ROI) and zoom on each of the ROI, completed with the software measurement windows and tables with the obtained values.

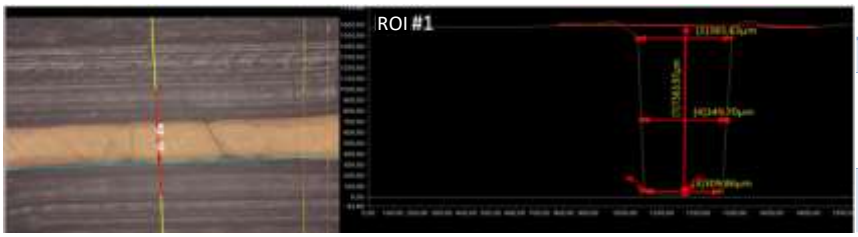

ROI 1		Channel 1
Length (µm)		1,563.97
Width (µm)	Top	385.63
	Middle	349.70
	Down	309.86
Angle (Deg) (L / R)		90.77 / 94.12

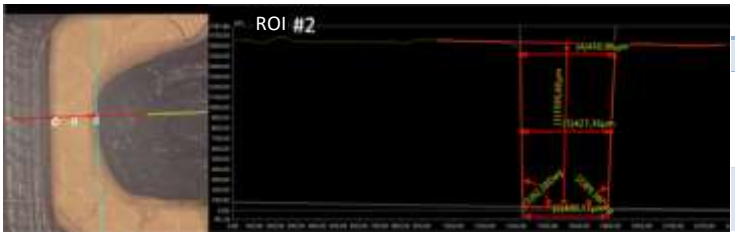

ROI 2		Channel 1
Length (µm)		1,595.60
Width (µm)	Top	450.96
	Middle	427.36
	Down	400.17
Angle (Deg) (L / R)		93.38 / 89.38

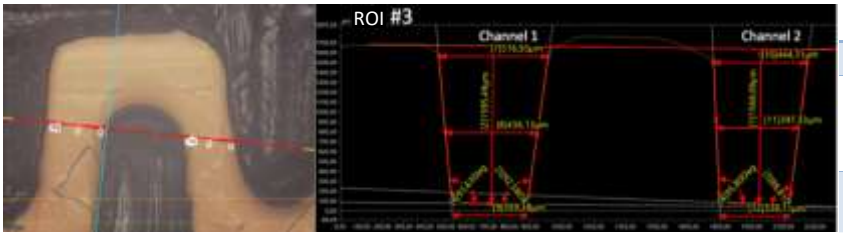

ROI 3		Channel 1	Channel 2
Length (µm)		1,594.49	1,568.09
Width (µm)	Top	516.93	444.31
	Middle	436.13	397.33
	Down	359.38	338.11
Angle (Deg) (L / R)		93.63 / 92.58	95.80 / 88.81

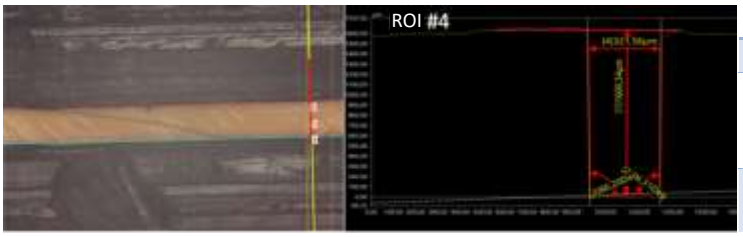

ROI 4		Channel 1
Length (µm)		1,600.34
Width (µm)	Top	321.56
	Middle	
	Down	
Angle (Deg) (L / R)		86.20 / 94.34

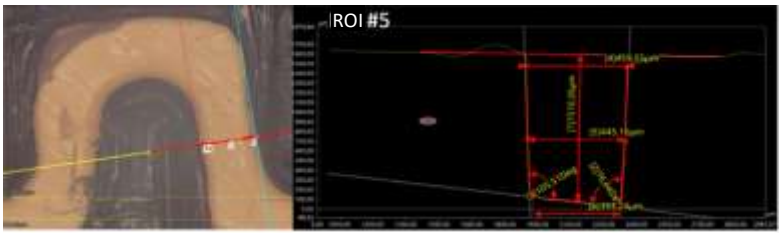

ROI 5		Channel 1
Length (µm)		1,510.34
Width (µm)	Top	449.55
	Middle	445.17
	Down	393.24
Angle (Deg) (L / R)		105.51 / 76.64

Figure S4-4: Digital microscopy observations of the PEEK chip: whole chip (including the localization of the 5 ROI) and zoom on each of the ROI, completed with the software measurement windows and tables with the obtained values.

S5 Confocal laser scanning microscope on PEEK chip for channel characteristic measurements

Thanks to PEEK autofluorescence, PEEK chip has also been characterized by confocal laser scanning microscope on two ROI (Figure S5-1, Figure S5-2, Figure S5-3)

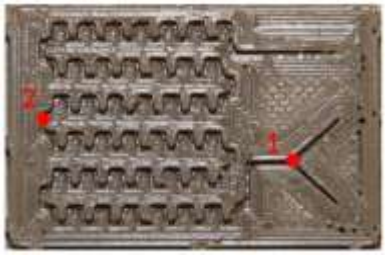

Figure S5-1: PEEK chip overall view with the two ROI observed by confocal laser scanning microscope

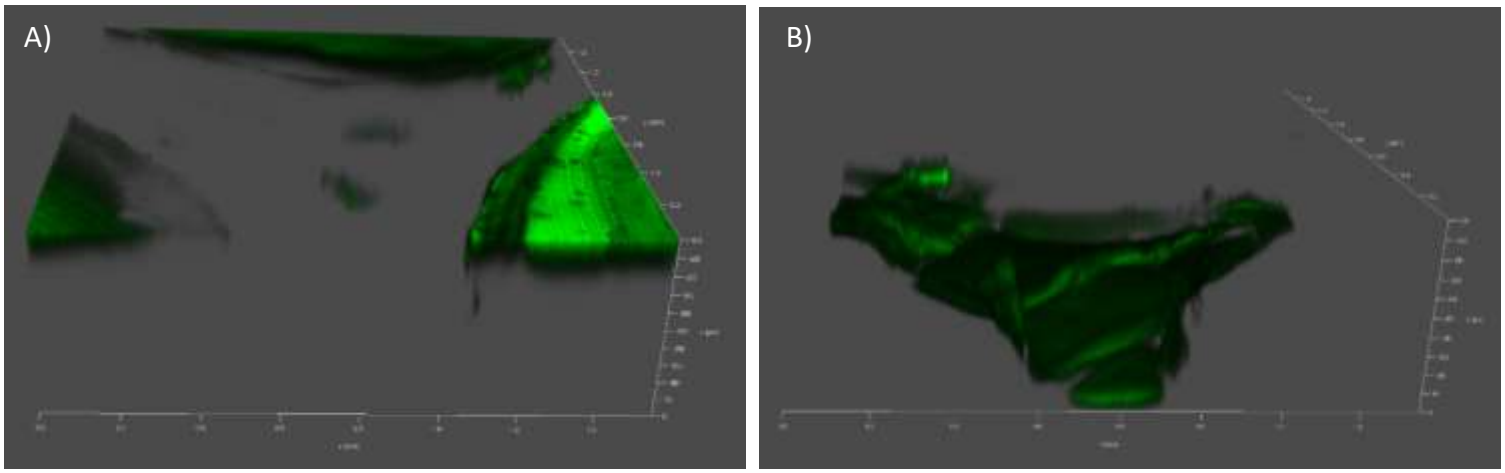

Figure S5-2: A) Top and B) down view by S4 Confocal laser scanning microscope of the ROI 1

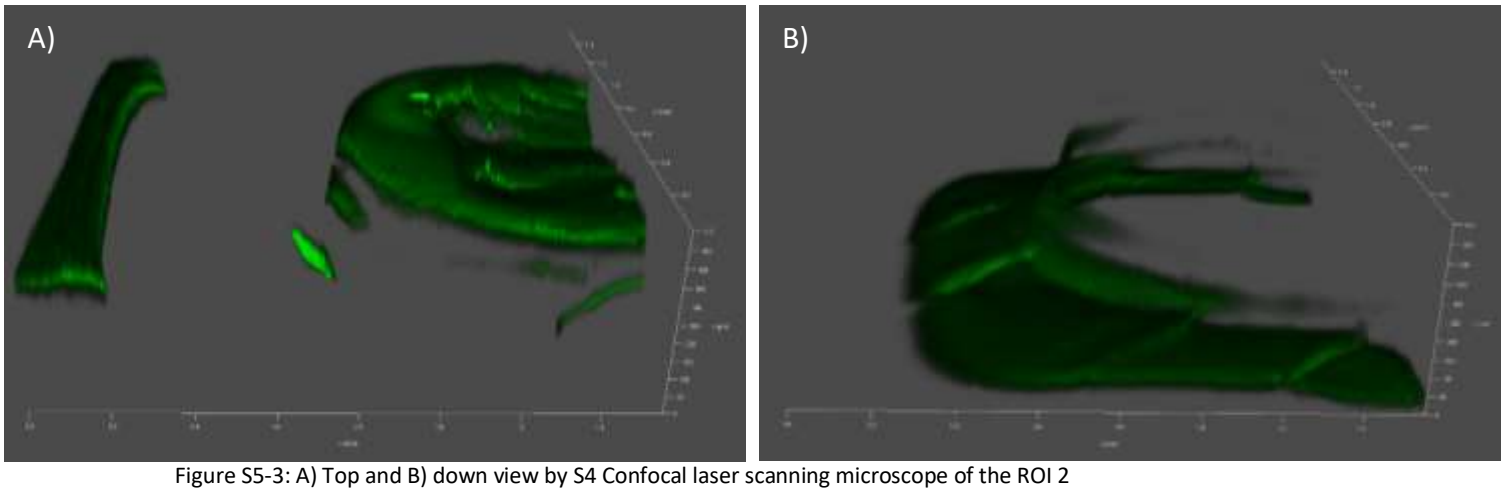

Figure S5-3: A) Top and B) down view by S4 Confocal laser scanning microscope of the ROI 2

S6 Statistical analysis

As explained in the text, different statistical tools have been used to compare LNC formulated with (i) the PEEK and Si/Glass chips and (ii) the PEEK chip with two different flowrates. The objective was to determine if the chip material and the flowrate had any impact on the formulated LNCs.
Three complementary methods are used:

1. Violin plots allow a graphical representation of the raw data, median and interquartile range of each variable, visually showing any significative difference;
2. Passing-Bablok regression check the hypothesis of supposed linearity between the two variables Y_i and X_i ($Y_i = \alpha + \beta X_i$);
3. Bland-Altman plot check the agreement of obtained measures and allow detecting any incoherent value.

▪ PEEK vs Si/Glass

To compare the two different chips, Si/Glass chip has been selected as the reference chip (X_i) due to the best control of the width and wall linearity of its channels (the PEEK chip being Y_i).

The Passing-Bablok regression study confirms the absence of significative difference between the PEEK and the Si/Glass chips. Indeed, Figure S6-1 shows that the slope is nearly one, and the confidence interval (CI) upper and lower bounds surround the value 1, meaning there is no proportional error. Furthermore, for the intercept, CI bounds surround the value 0, meaning there is no systematic error.

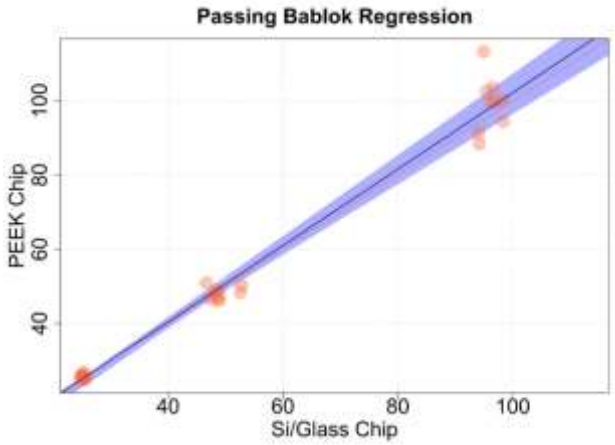

	Est*	LCI*	UCI*
Intercept (α)	-0.831	-4.247	1.685
Slope (β)	1.030	0.947	1.101

*Est: estimated value; LCI: 95% lower confidence interval; UCI: 95% upper confidence interval

Figure S6-1: Sizes of the LNC formulated with PEEK vs Si/Glass chips. Symbols represent experimental couples. The full line shows a Passing-Bablok Regression and the dotted line figures out the identity relation. Size are in nm. The 95% confidence bounds are calculated by the boostrap method (colored area).

In order to consolidate this result, a Bland-Altman analysis has been used to compare result agreement (Figure S6-2). It shows, for each targeted size, in ordinate the size difference (X_i - Y_i) and in abscissa the average size (X_i + Y_i)/2 obtained for a specific condition. It shows a good homogeneity and dispersion of the obtained sizes for all the targeted sizes. However, this analysis highlights the presence of an incoherent result: one of the LNC 100 formulations with Si/Glass chip had a size above 110 nm, while all the other sizes are below 103 nm. Excluding

this specific point, all measurements are within 10% around the median, and even within 5% for the LNC 25.

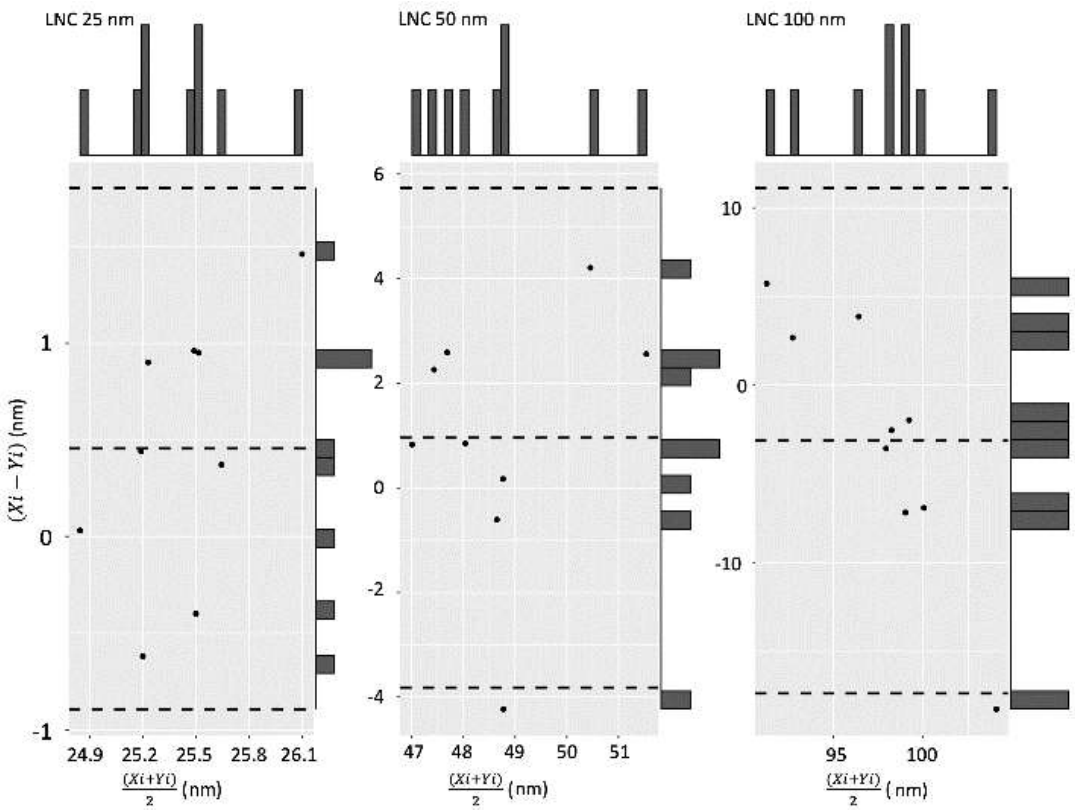

Figure S6-2: Bland-Altman analysis (Si/Glass vs PEEK) for each targeted size (25, 50 and 100 nm). The abscissa axis represents the average size (X_i+Y_i)/2 (with X_i for Si/Glass size and Y_i for PEEK size). The ordinate axis represents the size difference (X_i - Y_i) obtained for a specific condition *i*. Bar charts on the right and the top show the occurrence of those values. Upper and lower Dashed lines represent the upper and lower bound of the 95% confidence interval.

- Low vs High flow rate

To go further in the perspective of a "scaled-up" production, the same analysis was carried out to compare two different flow rates. An increase by a factor 5 was tested. Going above that value could damage chips and trigger leaks. Low flow rate (2.1 m/min) has been selected as the reference (X_i), while the high flow rate (10.5 ml/min) is Y_i.

Figure S6-3 compares results obtained for *D*Hz and PDI at two total flow rates (2.1 mL/min for the lowest and 10.5 mL/min for the highest). Results for LNC 25 suggest no significant difference for sizes and PDI. Same observations can be done for LNC 50 and LNC 100 PDI, but this is less obvious for sizes: LNCs formulated with high flow rate seem slightly smaller than at low flow rate for targeted size over 50 nm.
Passing-Bablok regression (Figure S6-4) confirms the previous observation: with a slope value lower than 1 (between 0.961 and 0.996), a (small) proportional error is attested. However, the intercept value demonstrates the absence of systematic error. Thus, it appears that sizes are slightly smaller when increasing the flow rate, but this drop stays below 5%, which is acceptable.
Bland-Altman analysis (Figure S6-5) shows once again a good homogeneity and dispersion of the obtained sizes for all LNCs, with all measurements within 6% around the median.

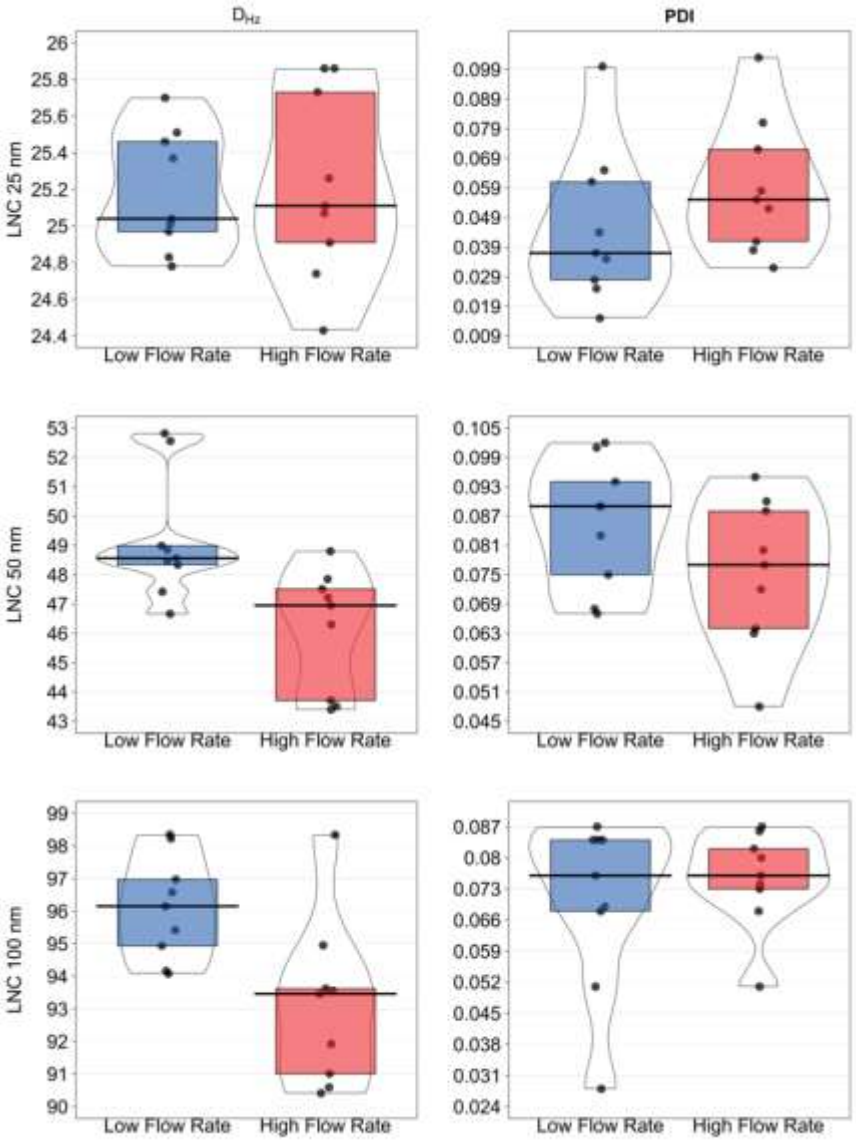

Figure S6-3: Violin plots of DHz and PDI for LNCs formulations obtained with PEEK chip at low (2.1 ml/min) and high flow rate (10.5 ml/min). Each boxplot introduces four elements: black points represent raw data, the horizontal black line represents the median, the bean represents a smoothed density and colored rectangles represent the interquartile range.

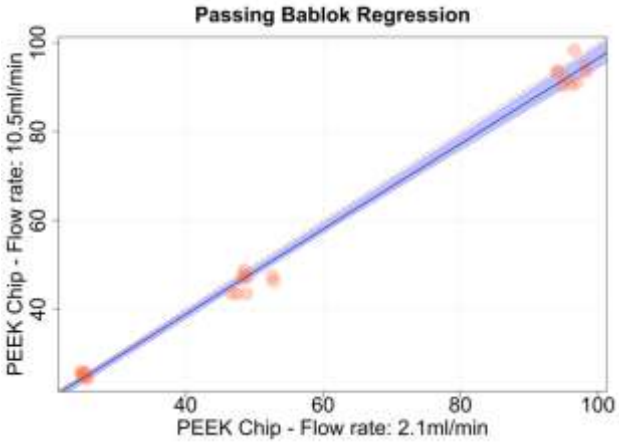

	Est	LCI	UCI
Intercept	-0.382	-1.477	1.902
Slope	0.961	0.927	0.996

*Est: estimated value; LCI: 95% lower confidence interval; UCI: 95% upper confidence interval

Figure S6-4: Sizes of the LNC formulated with high vs low flow rates. Symbols represent experimental couples. The full line shows a Passing-Bablok Regression and the dotted line figures out the identity relation. Size are in nm. The 95% confidence bounds are calculated by the bootstrap method (colored area).

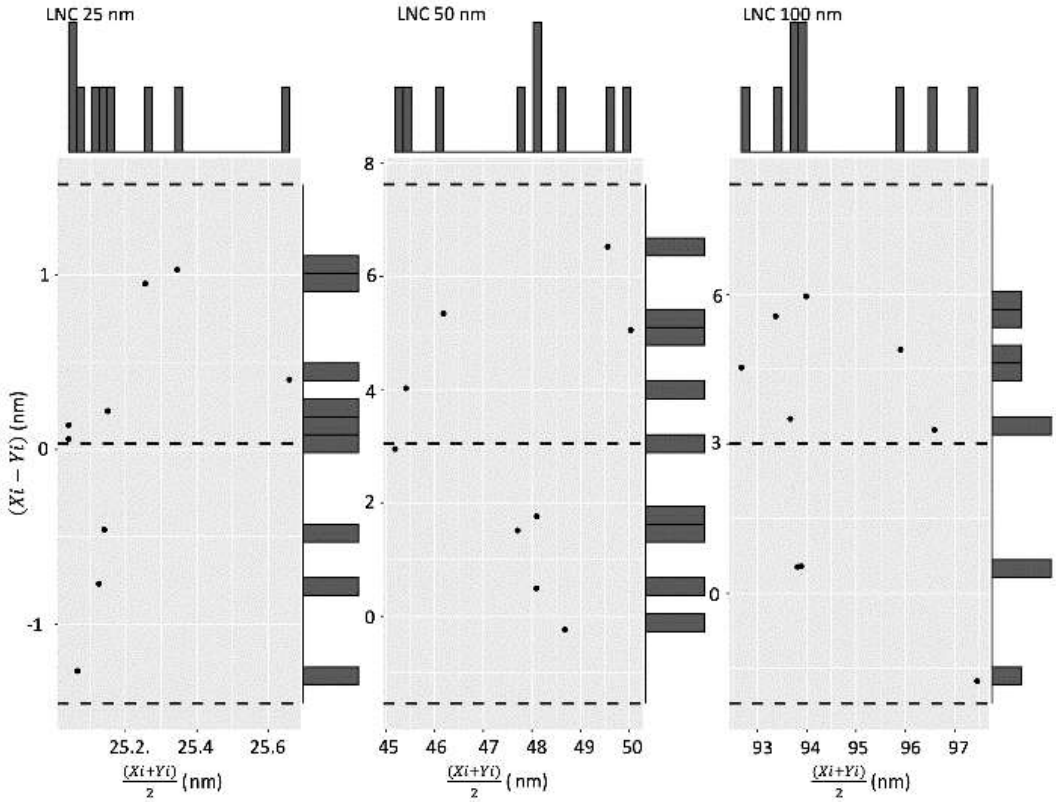

Figure S6-5: Fig 13: Bland-Altman analysis (low vs high flow rate) for each targeted size (25, 50 and 100 nm). The abscissa axis represents the average size (X_i+Y_i)/2 (with X_i for low and Y_i for high flow rate sizes). The ordinate axis represents the size difference (X_i - Y_i) obtained for a specific condition *i*. Bar charts on the right and the top show the occurrence of those values. Upper and lower Dashed lines represent the upper and lower bound of the 95% confidence interval.

S7 Small Angle X-ray Scattering (SAXS) data treatment and comparison

Well-known LNC-PIC batch suspensions were used to collect their SAXS intensity signal using classical glass-borosilicate capillaries with 1.5 mm diameter and 10 µm thick walls. Figure S7-1A shows the raw intensity data (in arbitrary units, a.u.) plotted on a log-log scale and obtained after radial averaging from the 2D detector multiple acquisitions (time averaged 10 × 500 ms), using a mask for the beam stop position that blocks the transmitted beam and dead pixels. A correction was used for pixels different efficiencies. Background measured with the X-ray shutter closed was negligible. SAXS intensity curves, plotted as a function of the scattering vector Q (in $Å^{-1}$), were obtained applying the standard beam-line corrections to reach an absolute scale (i.e. scattering cross section per scattering volume, in cm^{-1}) based on the measurement of the reference scattering intensity of pure water. The green symbols and curve in Figure S7-1A correspond to the raw measurements within 6% around the median and is mostly due to air and instrument window scatterings. For diluted samples, such contributions dominate all the intensity curves at low Q values. The water filled capillary raw signal (blue symbols and curve) is shown on the Figure S7-1A as well as the reference water signal (light grey symbols and curve around 0.0168 cm^{-1}) obtained after subtraction of the glass capillary signal and other beam-line corrections to obtain cm^{-1} units. Similarly, the SAXS signal in $cm^{-1}$of an LNC 25 nm PIC batch suspension diluted at 1% (w/w) was also plotted (red symbols and curve). The sample holder and solvent scattering (water isothermal compressibility signal) are mainly responsible for the scattering at large Q values and were subtracted from the data.

In order to compare the SAXS signal from diluted LNC suspensions measured in the microfluidic chip and in classical capillaries, the same suspension was measured in both environments at rest. The microfluidic chip was totally filled with the suspension used previously, and measurements were carried out through the microfluidic chip in the channel section accessible after the Y junction. The raw signal is plotted with black symbols and line in Figure S7-1B and it is identical to the one measured within capillaries in the low Q range (Figure S7-1A). On the contrary, the large Q range shows a slightly higher intensity due to an increase of the cell wall contribution and solvent scattering amount. Nevertheless, the same trend appears for the raw signal measured within the microfluidic chip filled with pure water (blue symbols and line), so that after subtraction of all these contributions (air, instrument windows scattering, sample holder and solvent scattering), the LNC SAXS curve measured within the microfluidic chip is identical to the one measured in the capillary (Figure S7-1). The best fits to the SAXS data are plotted with solid lines on top of the corresponding data. The model used is based on a spherical particle with a core-shell structure form factor and a hard sphere model for inter particles interactions using the Percus-Yevick closure structure factor. Excellent fits were obtained with a fixed electron density for the solvent (0.334 $Å^{-3}$) and the resulting electron density profile is plotted in Figure S6-2A. Moreover, the model also fits the size distribution of the core radius and shell thickness in the form of a log-normal and a normal distribution respectively (see Figure S6-2B). Lastly, data are in agreement with other experimental LNC determination, such as calculated electron densities from pure materials and sample composition (Table S7-1: reference values calculated for the pure formulation ingredients that composes the samples of the SAXS analysesTable S7-1).

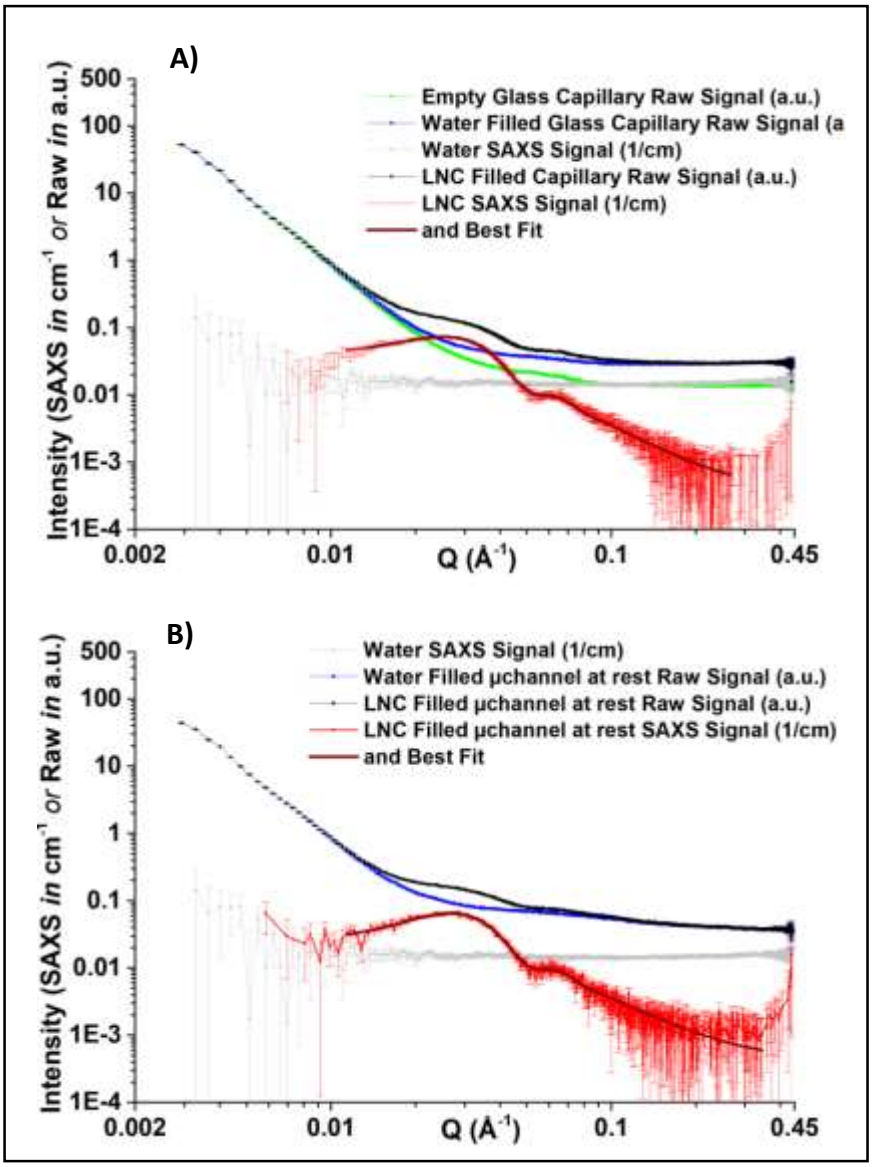

Figure S7-1: A) SAXS raw signal (a.u.) and SAXS intensity (in absolute scale units, cm-1) curves plotted as a function of the scattering vector on a log-log scale for measurements carried out within classical borosilicate glass capillaries (black and red dots, respectively). The black curve is the raw signal of the LNC 25 nm suspension at 1% (w/w). The Blue and green curves correspond for all plots to the raw signal collected with pure water and for air, respectively. The grey curve corresponds to measured pure water scattering in cm^{-1} and is plotted on all graphs as a guide to the eyes; B) corresponds to the same suspensions measured at rest in the microfluidic channel of the Si/Glass chip, 4 mm away from the Y junction (see Fig. 4C). The blue curve raw signal corresponds to the water filled channel and the black curve to the raw signal of the LNC suspension. In both cases, after proper treatments, the LNC suspension SAXS curve was obtained and plotted in red with its best fit to the data (black line).

Table S7-1: reference values calculated for the pure formulation ingredients that composes the samples of the SAXS analyses

Molecule, Segment	*Composition*	*M, Molar mass (g/mol)*	*d*, Volume density ($g.cm^{-3}$)	*X-ray (λ=1Å)* ρb, Scattering length density ($x10^{-6}Å^{-2}$)	*X-ray (λ=1Å)* ρ_e, Electron density ($Å^{-3}$)
Water	**2H;O**	**18.015**	**0.998**	**9.42**	**0.334**
Oil (Labrafac, *WL1349*)	**22H;14C;6O**	**302.15**	**0.945**	**8.64**	**0.307**
hydrophilic segment	5H;6C;6O		1.1	9.62	0.341
hydrophobic segments	17H;8C		0.684	6.67	0.237
Surfactant (Kolliphor HS15)	**96H ;48C ;17O**	**944.53**	**1.048**	**9.8**	**0.348**
hydrophilic segment	61H ;31C ;17O	239.19	1.116	10.3	0.366
hydrophobic segments	35H ;17C	705.34	0.847	8.23	0.292
Co-Surfactant (Span 80)	**44H;24C;6O**	**428.6**	**0.986**	**9.23**	**0.328**
hydrophilic segment	11H;7C;6O	191.08	1.03	9.25	0.328
hydrophobic segments	33H;17C	237.2	0.95	9.18	0.326

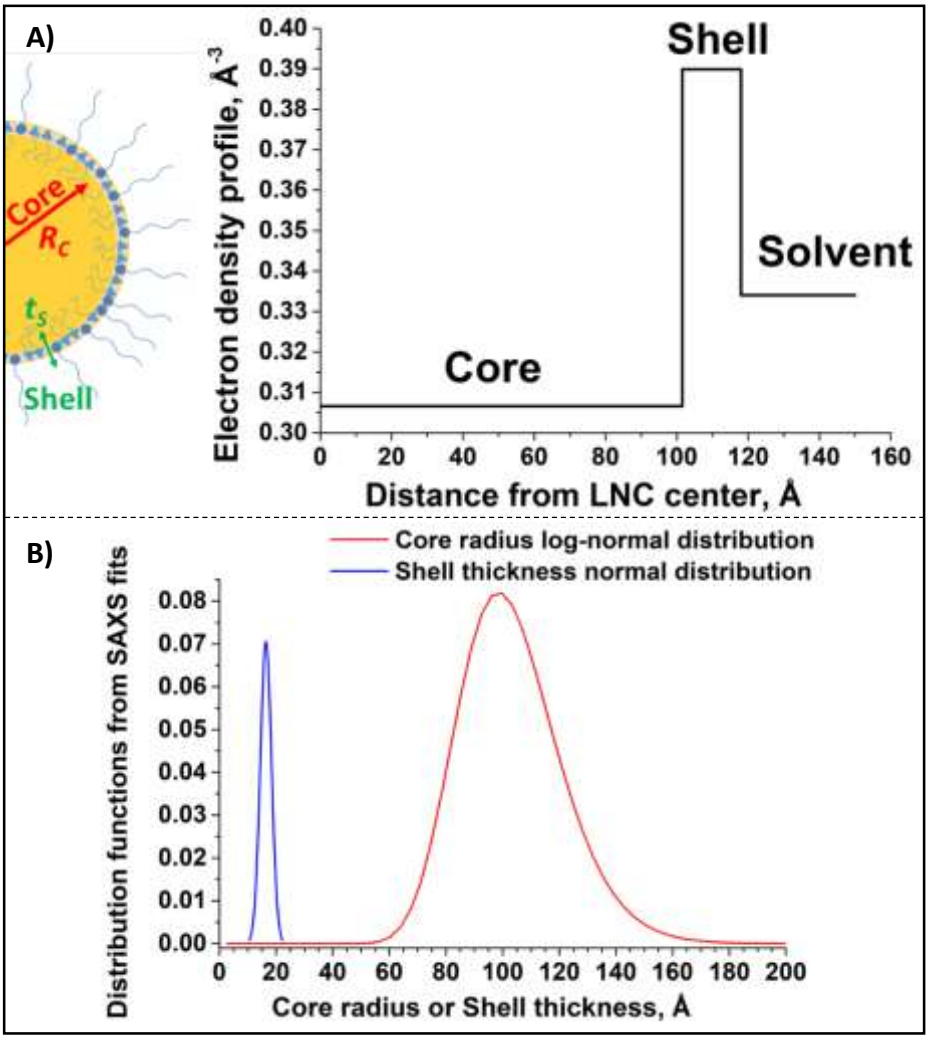

Figure S7-2: A) Electron density profile corresponding to the fit presented in Figure S7-1A for diluted LNC 25nm particles with a sketch representing a LNC; B) Distribution functions obtained from the fit, for the core radius (log-normal distribution) and shell thickness (normal distribution).

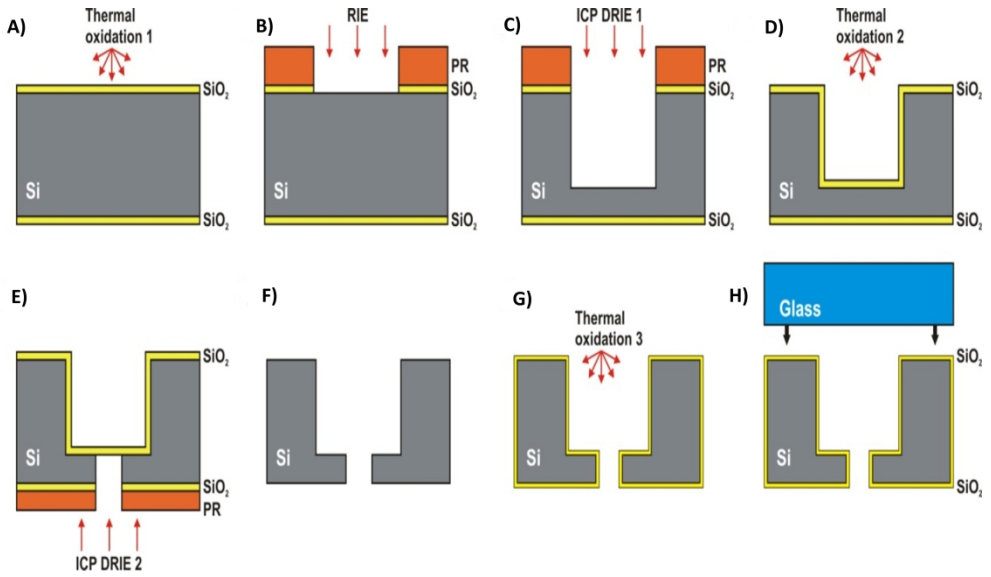

Fig 1: Fabrication process of Si-Glass microfluidic chip, combining the DRIE of silicon and anodic bonding: A) Thermal oxidation of Si, B) photolithography and dry etching of SiO2 mask, C) DRIE of microchannel, D) stripping of the masks and second thermal oxidation, E) back-side DRIE of via-holes, F) stripping of the masks, G) thermal oxidation (Si surface passivation), and H) anodic bonding to glass lid.

338x190mm (300 x 300 DPI)

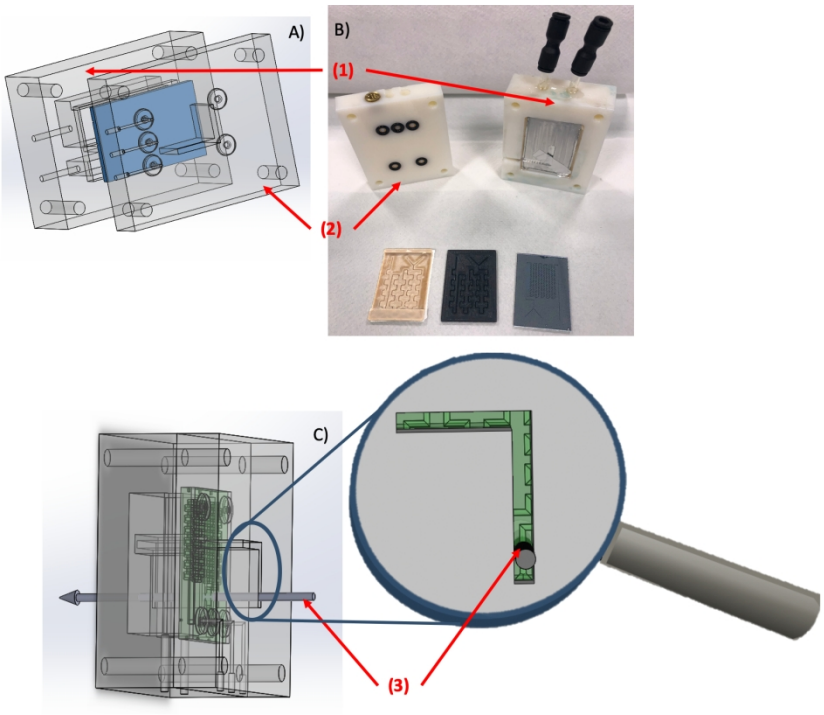

Fig 2: "All-in-one" plugging and heating device. CAD drawing (A) and picture (B) of the heating part called "waterblock" (1) and of the connector part (2). SAXS implementation (C) with the representation of the X-ray beam path (3) (see section 2.5.2. SAXS analysis for more details).

254x190mm (200 x 200 DPI)

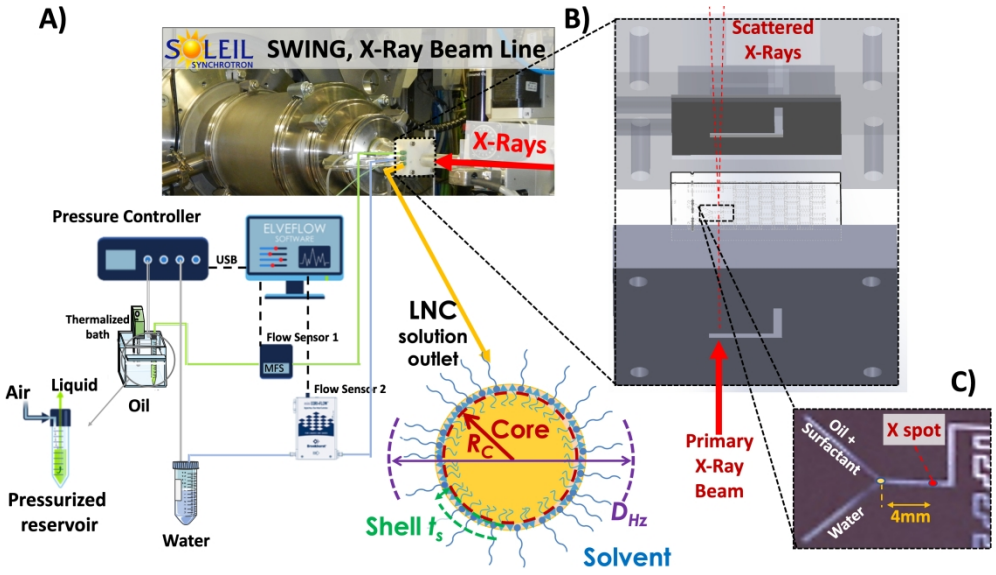

Fig 3: A) Integration of the microfluidic formulation pilot in the SAXS environment at the SOLEIL synchrotron SWING beamline for in situ characterization of the LNC structure and their characteristics as the shell thickness (ts), the hydrodynamic diameter (DHz) and the core radius (Rc) ; B) Representation of the microfluidic setup composed of the chip mounted inside the waterblock connector and C) Position of the X-ray beam.

338x190mm (300 x 300 DPI)

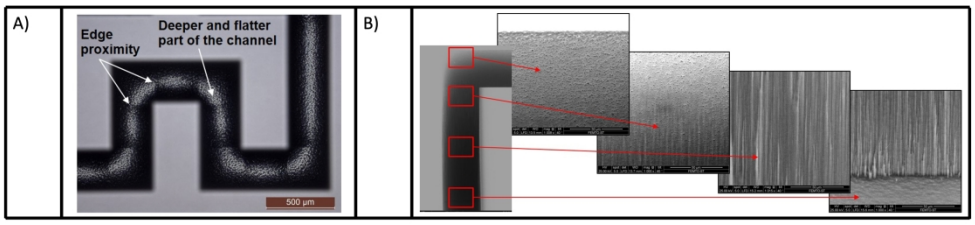

Fig 4: SEM pictures for the characterization of the microchannel in terms of depth uniformity and surface quality: A) Corrugation of the bottom surface due to very local variation of etch rate, B) Evolution of the sidewall quality along the total depth of 1.5 mm (SEM tilted view).

338x190mm (300 x 300 DPI)

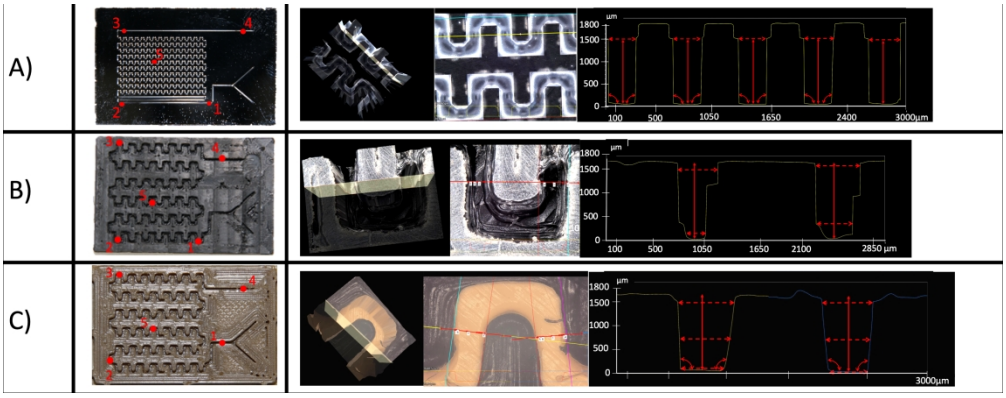

Fig 5: 2D/3D microscopic observations of 90° elbows of A) the Si/Glass chip, B) the ABS chip and C) the PEEK chip. Each Region Of Interest (ROI) are presented for each chip and numbered from 1 to 5. Each chip was observed on the RIO number 5 on this present example.

451x175mm (225 x 225 DPI)

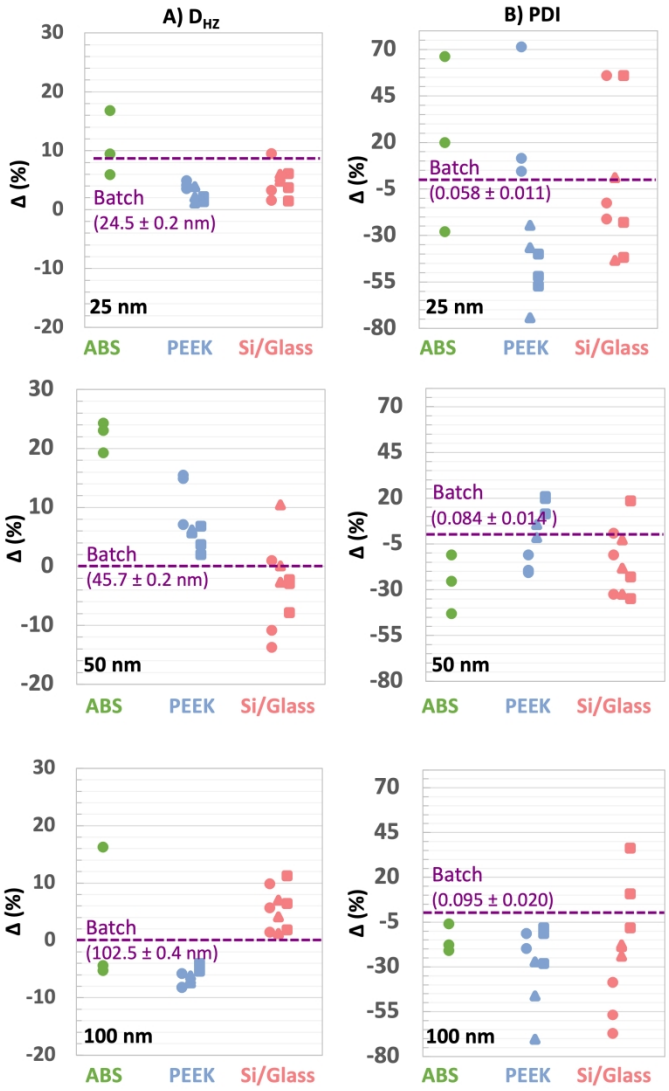

Fig 6: Comparison of (A) DHz and (B) PDI for three targeted sizes indicated in the figures (25, 50 and 100 nm) using the PIC batch and microfluidic processes. Results obtained with the batch process are used as references (purple dashed lines). Results obtained with the three different chips are represented with different colored symbols: ABS (green), PEEK (blue) and Si/Glass (pink). Independent organic stock solutions were prepared for each targeted size and are represented by various symbols (circles, triangles, squares) with three "start and stop" for each one.

190x338mm (270 x 270 DPI)

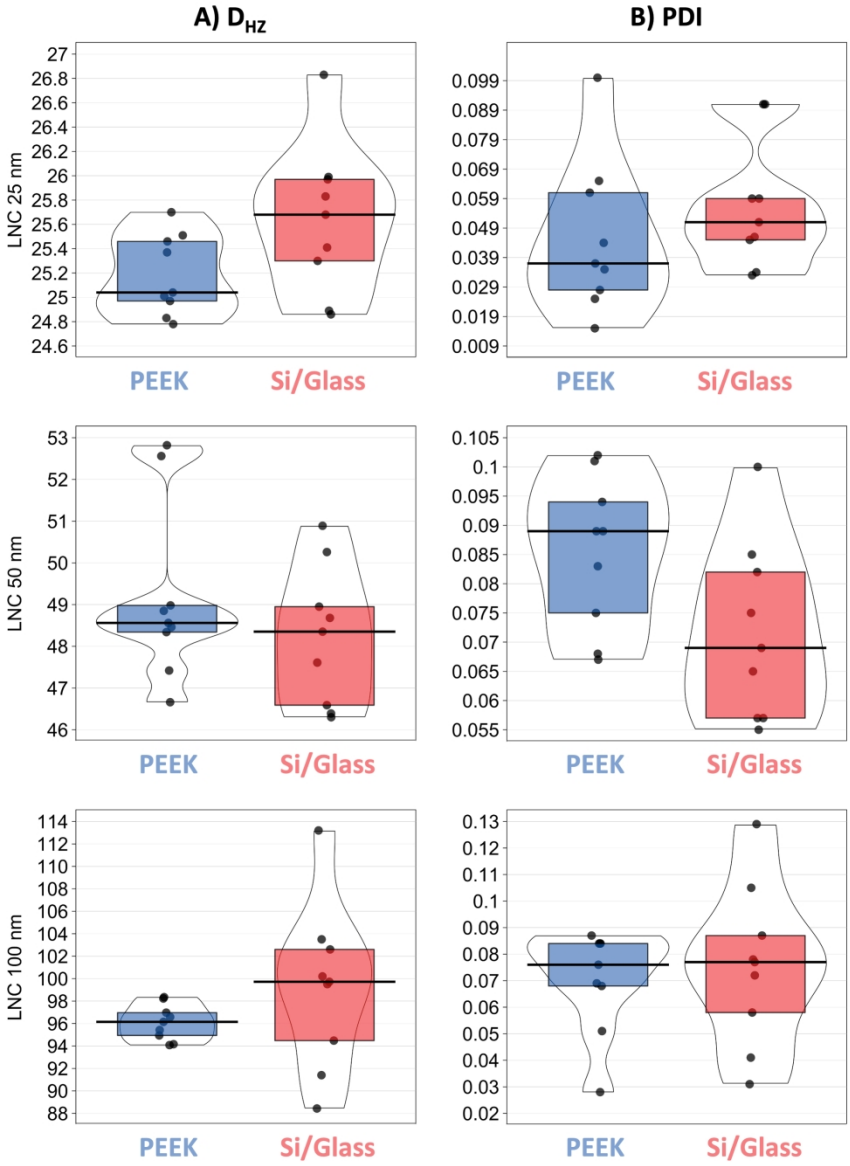

Fig 7: Violin plots of (A) DHZ and (B) PDI for LNC formulations obtained with PEEK (blue) and Si/Glass (pink) chips. Each boxplot introduces four elements: black points represent raw data, the horizontal black line represents the median, the bean represents a smoothed density and colored rectangles represent the interquartile range.

190x265mm (300 x 300 DPI)

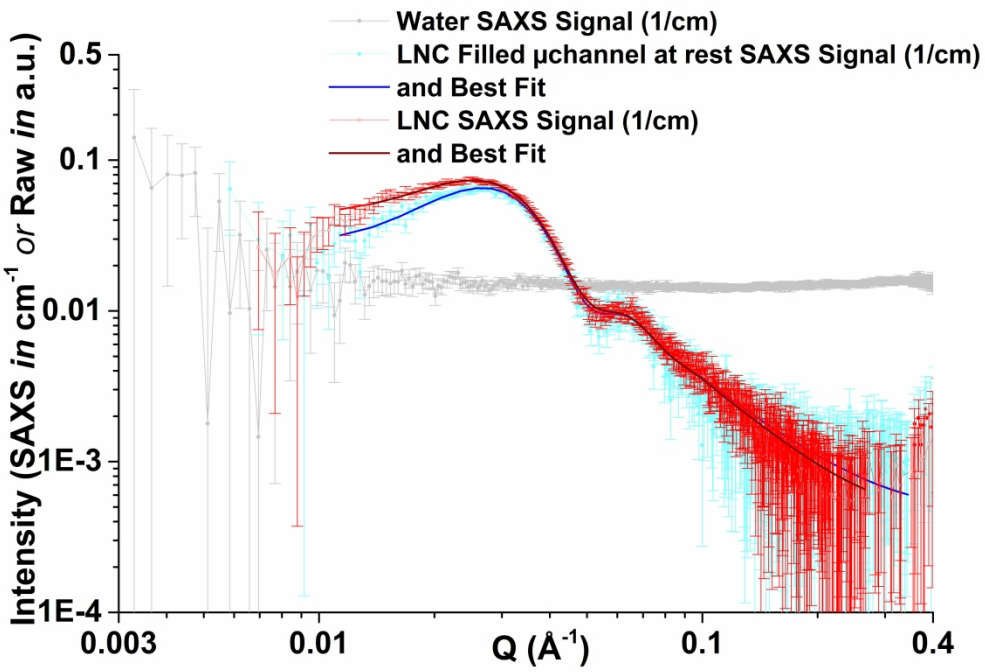

Fig 8: SAXS intensity (in absolute scale units, cm-1) curves plotted as a function of the scattering vector on a log-log scale for measurements carried out within classical borosilicate glass capillaries (red dots) of the LNCs 25 nm suspension at 1% (w/w). The cyan dots correspond to the same suspension measured at rest in the microfluidic channel of the Si/Glass chip (4 mm away from the Y junction (see Fig. 4C). The best fits to the data are plotted on top of the two SAXS data curves in cm-1 and correspond to the wine-red and blue lines, respectively). The grey curve corresponds to measured pure water scattering (curve around 0.0168 cm-1) and is plotted as a guide to the eyes. Raw data curves are shown in the SI (Fig S6-2).

296x209mm (300 x 300 DPI)

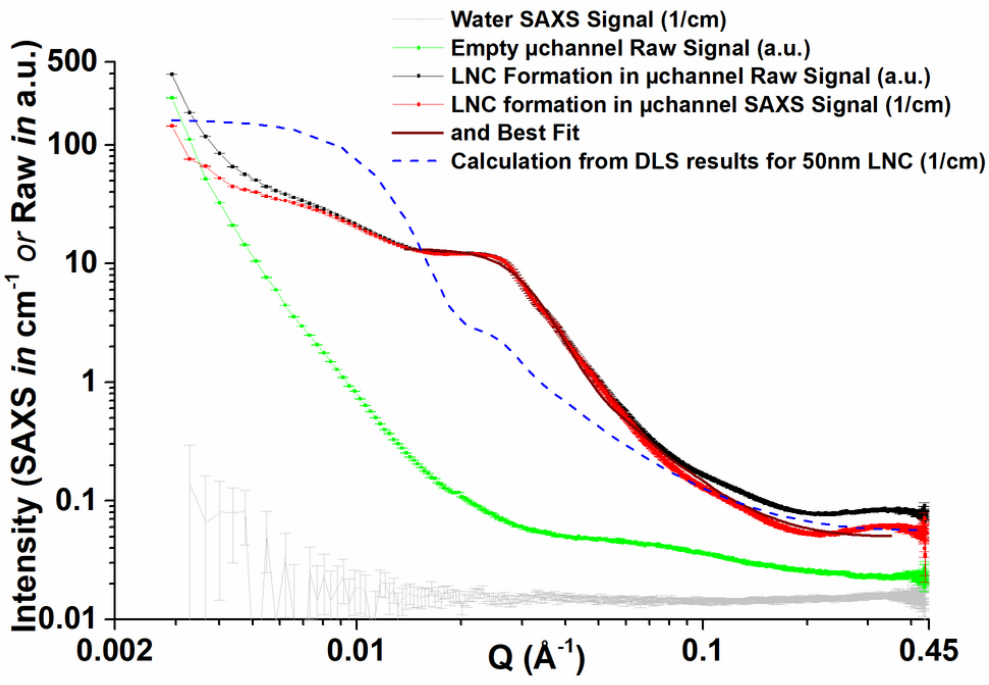

Fig 9: Raw signals and SAXS curve measurements carried out in the microfluidic channel under flow during formulation of LNCs 50 nm at 5% (w/w). The SAXS curve and its best fit are plotted with red dots and line and a brown line, respectively. Other color codes are identical to the ones used previously. The dashed line is the SAXS curve calculated for stable LNC core-shell particles (RC=48.5 nm, PDI ~ 0.07 and same values as previously for other parameters).

82x58mm (300 x 300 DPI)

Credit author statements

Nicolas ROLLEY
Conceptualization, Methodology, Statistical analysis, Investigation, Data Curation and treatment, Writing – Original, Draft, Writing - Review & Editing

Marie BONNIN
Conceptualization, Resources, Writing - Review & Editing, Supervision

Guillaume LEFEBVRE
Conceptualization, Resources, Investigation, Writing - Review & Editing, Supervision

Sylvain VERRON
Conceptualization, Methodology, Resources, Writing - Review & Editing

Sylwester BARGIEL
Conceptualization, Methodology, Investigation, Resources, Writing - Review & Editing

Laurent ROBERT
Conceptualization, Methodology, Investigation, Resources, Writing - Review & Editing

Jérémie RIOU
Conceptualization, Methodology, Statistical analysis, Resources, Writing - Review & Editing

Carl SIMONSSON
Conceptualization, Methodology, Resources, Writing - Review & Editing

Thomas BIZIEN
Conceptualization, Methodology, Investigation, Resources, Writing - Review & Editing

Jean-Christophe GIMEL
Methodology, Investigation, Resources, Writing - Review & Editing

Jean-Pierre BENOIT
Writing - Review & Editing, Project administration, Funding acquisition.

Guillaume BROTONS
Conceptualization, Methodology, Resources, Investigations, Data Curation and treatment, Writing - Review & Editing, Supervision.

Brice CALVIGNAC
Conceptualization, Methodology, Resources, Investigations, Data Curation and treatment, Writing - Review & Editing, Project administration, Funding acquisition, Supervision